Title: Achieving tolerant CO_2 electro-reduction catalyst in real water matrix

Authors: Da Hye Won, Hyeyoung Shin, Min Wook Chung, Hyejin Jung, Keun Hwa Chae, Hyung-Suk Oh, Yun Jeong Hwang, Byoung Koun Min

PII: S0926-3373(19)30707-6
DOI: https://doi.org/10.1016/j.apcatb.2019.117961
Article Number: 117961

Reference: APCATB 117961

To appear in: *Applied Catalysis B: Environmental*

Received date: 17 December 2018
Revised date: 11 July 2019
Accepted date: 12 July 2019

Please cite this article as: Won DH, Shin H, Chung MW, Jung H, Chae KH, Oh H-Suk, Hwang YJ, Min BK, Achieving tolerant CO_2 electro-reduction catalyst in real water matrix, *Applied Catalysis B: Environmental* (2019), https://doi.org/10.1016/j.apcatb.2019.117961

Achieving tolerant CO_2 electro-reduction catalyst in real water matrix

Da Hye Won,[a] Hyeyoung Shin,[b] Min Wook Chung,[c] Hyejin Jung,[a] Keun Hwa Chae,[d] Hyung-Suk Oh,[a] Yun Jeong Hwang[a,e,*], Byoung Koun Min[a,f,*]

[a]Clean Energy Research Center, Korea Institute of Science and Technology, Hwarang-ro 14-gil 5, Seongbuk-gu, Seoul 02792, Republic of Korea

[b]Materials and Process Simulation Center, California Institute of Technology, Pasadena, California 91125, USA

[c]School of Materials Science and Engineering, Gwangju Institute of Science and Technology, 123 Cheomdangwagi-ro, Buk-gu, Gwangju 61005, Republic of Korea

[d]Advanced Analysis Center, Korea Institute of Science and Technology, Hwarang-ro 14-gil 5, Seongbuk-gu, Seoul 02792, Republic of Korea

[e]College of Engineering, Yonsei University, 50 Yonsei-ro, Seodaemun-gu, Seoul 03722, Republic of Korea

[f]Green School, Korea University, Anam-ro 145, Seongbuk-gu, Seoul 02841, Republic of Korea

[*]Corresponding authors:

bkmin@kist.re.kr (B.K. Min), Tel: +82-2-958-5853, Fax: +82-2-958-5809

yjhwang@kist.re.kr (Y.J. Hwang), Tel: +82-2-958-5227, Fax: +82-2-958-5809

Graphical abstract

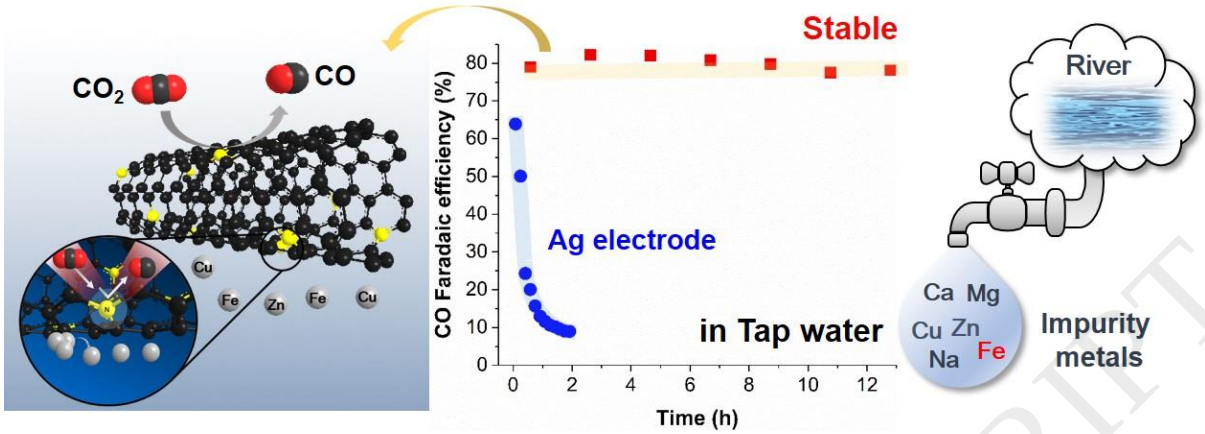

Highlights

- Electro-reduction of CO_2 was performed in real water matrix (tap water) conditions.
- Iron was found to be the most detrimental element in silver catalyzed CO_2 electro-reduction.
- Nitrogen doped carbon based material was designed to be a stable model catalyst in real water.
- Stable performance was tested for an unprecedented long-time of 120 hours in tap water media.

Abstract

It is essential to develop durable catalysts in real water matrix to achieve practical application of electrochemical CO_2 conversion technologies because use of only high-performing catalysts in well-refined environment cannot guarantee their feasibility in realistic conditions. Here, we report a design strategy for a catalyst, which shows excellent tolerance to deactivation factors, using a carbon-based material under more practical condition implemented by real tap water used in everyday life. Screening analyses elucidated the impurity group that can be deposited on the catalyst surface to impede the active sites such as copper, zinc, and especially iron, which are the main factors responsible for deactivation. Structural analysis of the modified nitrogen-doped carbon nanotube revealed tolerance to the investigated deactivation factors and showed stable performance in an unprecedented long-time of 120 hours in tap water media.

Keywords. Carbon dioxide, Carbon monoxide, Carbon material, Electrocatalyst, Tap water

1. Introduction

Artificial photosynthesis, which converts water and CO_2 into chemicals powered by sunlight, is the holy grail of sustainable development in terms of carbon cycle and chemical production.[1-3] Among the various strategies to realize this dream, one of the most highlighted way is to combine electrochemical CO_2 reduction with photovoltaic technology as a solar-chemical production. Since CO_2 reduction reaction (CO_2RR) involves sluggish kinetics as CO_2 is chemically stable, a bottleneck for the successful development of this system is to develop a suitable CO_2 reduction catalyst. Thus, most studies have focused on the development of high-performing catalysts through the modification of physical and/or chemical structures using various materials, generally metals (*e.g.*, Ag[4-9], Au[10-13], Cu[14-16], Sn[17-19], Pd[20,21], and Zn[22,23]). However, considering the important fact that this technology is destined for commercial and practical applications, in addition to the efficiency (*e.g.*, selectivity), the catalyst should also satisfy the feasibility of scaling up to improve its cost-effectiveness; more importantly, its long-term durability should be guaranteed first.

To date, many kinds of the state-of-the-art catalysts have been developed showing outstanding activities and selectivities, but their stabilities have been reported to be within hours or a maximum of hundred hours (Table S1).[5-12,17-19,22-28] To achieve high durability for practical application, the issue of deactivation of the metal catalyst should be first considered. However, no study has yet extensively focused on this issue. In many cases, a catalyst would be deactivated by the deposition of tightly bound intermediates (poisoning) or by the formation of a graphitic/or amorphous carbon layer (fouling).[8,12,29,30] In a recent report, however, an immediate

degradation of catalytic activity has been observed because of the external factors such as an electrolyte, one of the most basic component of the CO_2 electro-reduction system, in addition to the aforementioned internal factors.[31] For example, the representative metal-based catalyst for the CO_2RR such as Au, Ag, and Cu, are rapidly poisoned by trace metal impurities present even in an extremely refined electrolytes.[31] This suggests that further purification steps such as pre-electrolysis or metal-ion chelation are required to achieve catalyst stability, indicating an additional cost for pure water supply that hinders the industrialization of this technology. In other words, a good performing catalyst may not reproduce its ability in realistic conditions, which will be different from ideal laboratory-scale conditions. Therefore, to validate the feasibility of the developed catalysts in future application, practical approaches accompanied with an in-depth understanding of key deactivation factors derived from uncontrollable external factor are necessary.

In terms of feedstocks (*e.g.*, water) for massive production through large-scale solar-chemical production system, a plausible condition is to utilize real water matrix from river or ocean as industrial water (Fig. 1). As a first step in that direction, it can be reasonably attempted to use tap water as an electrolyte for CO_2 electro-reduction, because tap water can be considered as representative realistic water because of the similarity in the water quality standards for general purposes such as living, agriculture, and industry with respect to metal impurities.[32] A study on the phenomenon occurring in tap water is expected to provide clues to overcome anticipated difficulties faced in realistic water environments. To easily examine the influence of tap water on the catalytic performance, CO_2 reduction to CO would be an appropriate target reaction because of its simple reaction steps and easy detection compared with those for other products. Furthermore, CO is a useful chemical itself

because it can be used to produce higher-energy-density chemicals as a syn-gas with H_2.[33] Also, CO is a very important feedstock chemical to synthesize valued industrial reagent and building blocks in the synthesis of pharmaceuticals and other organic compounds (*e.g.*, polyurethane).[34,35]

Here, we report a one-step ahead approach for developing a durable CO_2 electro-reduction catalyst that can provide clues on how to overcome the anticipated difficulties in realistic conditions by distinctly focusing on the most basic component of electrochemical CO_2 conversion system, *i.e.*, the water media. Our investigation explores (i) the performance profile of a standard metal electrode (here, Ag that catalyzes CO production) in a representative general-purpose water (here, ordinary tap water used in real-life); (ii) the cause of observed phenomena, *e.g.*, deactivation; and (iii) the design of a durable catalyst in realistic water media based on observation noted using the Ag example. Among the various components of tap water ranging from alkali earth metals to transition/post-transition metals, we systematically demonstrated which specific components were detrimental to the performance of the Ag electrode by classifying groups based on their properties. The results of screening analyses showed that the impurity groups that can be deposited on the surface such as Cu, Zn, and especially Fe are the main factors responsible for catalyst deactivation. Consequently, a short metal-free nitrogen-doped carbon nanotube (denoted as ball mill N-CNT) was designed and proposed as our durable catalyst because of its intrinsic resistance to carbon contamination (a well-known deactivation factor of metal catalysts that was also observed on Ag surface post-reaction) and more importantly, its less vulnerable active sites over the scope of CO_2 electro-reduction reaction.[36-43] As expected, the ball mill N-CNT showed a competitive and stable performance regardless of the water source, whether it be deionized water or tap water.

Furthermore, ball mill N-CNT exhibited remarkable tolerance to even harsher conditions containing tenfold to hundredfold higher metal impurity concentration relative to tap water, revealing a strong resistance against impurities that would inevitably be present in realistic water conditions.

2. Experimental

2.1 Synthesis

The Ag foil (99.998%, Alfa Aesar) prepared by mechanical polishing, cleaning, and drying was directly used as an electrode. Ball mill N-CNT was prepared by sequentially subjecting to ball milling, acid treatment, and N doping of as-purchased multi-wall CNTs (99%, Carbon nanotech). First, the CNT was mixed with MgO powder (heavy, Sigma-Aldrich) of 5 times higher mass and a 3 mm zirconia ball in a 250 mL Nalgene bottle. Ball milling was performed for 3 h at a rotating speed of 500 rpm at room temperature. Upon completion, pure HNO_3 (60%, Samchun) was poured into the as obtained powder and stirred for a while. The mixed solution was boiled for 3 h at 140 °C in a reflux system to dissolve MgO and introduce oxygen functional groups onto the carbon surface for facile N-doping. After the acid treatment, the powder was filtered using a membrane filter, rinsed several times with deionized water, and dried in an oven (oxidized CNT). For N-doping, a certain amount of oxidized CNTs was blended with double amount of dicyandiamide (99%, Aldrich) in deionized water and ultra-sonicated for over 15 min. The solvent was evaporated using a rotary evaporator equipped with a water bath and a vacuum pump. The remaining powder was gathered and then heat-treated under a N_2 atmosphere at 850 °C for 3 h (ball mill N-CNT). To further investigate the correlation between each preparation process and the catalytic performance, two additional N-doped CNT catalysts were prepared: N-oxi-CNT and N-CNT. Of the above-mentioned three steps for ball mill N-CNT, only acid treatment and N-

doping processes were performed for N-oxi-CNT preparation. The N-CNT catalyst was prepared using the N-doping process only.

To utilize the synthesized powder as a cathode catalyst for CO_2RR, a catalyst ink solution was prepared by the following procedure: 10 mg of the catalyst was well dispersed in 1 mL of a mixed solution of 2-propanol, deionized water, and a Nafion solution (5 wt.% in lower aliphatic alcohols and water, Aldrich). The prepared ink solution was gradually drop-casted onto a glassy carbon substrate (Alfa Aesar) in a dry room until the loading amount of the catalyst reached 3 mg cm^{-2}.

2.2 Physical characterization

The various physical properties of the as-prepared and post-reaction catalysts were characterized by transmission electron microscopy (TEM), scanning transmission electron microscopy (STEM), energy-dispersive X-ray spectroscopy (EDX), Raman spectroscopy, X-ray photoelectron spectroscopy (XPS), elemental analyzer, and X-ray adsorption near-edge structure (XANES). The morphology of the as-prepared catalysts was first observed under TEM (Titan, FEI) at an accelerating voltage of 200 kV. The specific morphology and composition of the post-reaction catalysts were analyzed by STEM and EDX (Talos F200X, FEI). Raman spectroscopy was performed to measure the defects of the prepared carbon catalysts by using a 532 nm edge laser. The elemental composition (qualitative or quantitative) of the prepared CNT catalysts was determined using an elemental analyzer (FlaschEA 1112 for detecting the C, H, N, and Flash 2000 series for detecting O) according to the following method: the organic compound in a tin container (or a silver container for detecting O) is dropped into a high-temperature combustion chamber and/or a pyrolysis chamber to conduct dynamic flash combustion oxidation, followed by analysis of elements such as C, H, and N (or O) derived from the organic compound by column chromatography combined with a thermal conductivity detector. To further confirm the chemical structure of

the CNT catalysts, XPS was performed using an electron analyzer (SES100) at 510 eV photon energy of a linear undulator U6.8 (8A2 high-resolution photoemission spectroscopy, Pohang Accelerator Laboratory) and the spectrum of each catalyst was deconvoluted to reveal four different N structures. The atomic amount of the different N structures were determined by combining the quantitative amount of N doping, obtained from elemental analysis, and the relative concentrations of N structures, obtained from XPS results. The surface compositions of pristine and post-reaction catalysts (Ag electrode and ball mill N-CNT) were also analyzed by another XPS (PHI 5000 VersaProbe) by using monochromatic Al Kα at (1486.6 eV). Fe state on the ball mill N-CNT was further confirmed by observing the Fe *K*-edge (1D XRS KIST-PAL, Pohang Accelerator Laboratory).

2.3 Electrochemical CO_2 reduction

Electrochemical CO_2RR was performed with a potentiostat (Ivium Stat-potentiostat, Ivium Tech) in a two-compartment customized electrochemical cell (Fig. S1), where the cathode and anode regions were separated using an anion exchange membrane (Selemion AMV). The reactor had several inlets and outlets for passing CO_2 gas and inlets for injection of stock solution. A saturated calomel electrode (SCE) and a Pt foil (0.05 mm, 99.99%, Alfa Aesar) were used as the reference and counter electrodes, respectively. The as-prepared cathode catalysts (*i.e.*, Ag foil and N-doped CNT catalysts deposited on glassy carbon substrates) were used as the working electrode, with a geometric active area of 0.28 cm^2 (a circular shape of diameter 6 mm). The current density was normalized with respect to the geometric surface area of the cathode.

The catalytic performance was examined through step-potential electrolysis with periodic quantification of the gaseous products by on-line connected GC. The products from CO_2 electrolysis were CO and H_2 with a net total Faradaic efficiency of nearly 100%. The electrolyte used comprised CO_2-bubbled 0.5 M $KHCO_3$ (99.7%, Sigma-Aldrich) aqueous

solution (pH 7.4), which was prepared using two types of water: deionized water and common tap water (sourced from a service in Seoul, Korea). To observe the performance trends depending on the external conditions, the potential was applied at which the catalytic activity of each electrode was revealed to be the highest. The long-term operations were performed through sequentially programmed cycles involving an applied constant potential (E control) and a short period of the resting step (open cell) by using program of Iviumsoft. The potentials applied (relative to the SCE) were converted relative to the reversible hydrogen electrode (RHE) using the following equation: E (*vs.* RHE) = E (*vs.* SCE) + 0.214 + 0.059 V × pH. All the potentials were compensated for the *iR* loss.

Gas product analysis was *in situ* carried out with a GC (6500 GC, Young Lin Instrument Co. Ltd) directly connected to the reactor while conducting the electrochemical CO_2RR. The GC was equipped with a pulsed discharge ionization detector (PDD) and a capillary molecular sieve column (Restek, RT®-Msieve 5A), and used ultra-high purity He (99.9999%) as the carrier gas. During the measurement, CO_2 gas was continuously flowed through the electrochemical cell at a velocity of 20 mL min^{-1}.

2.4 *In situ* simulation test.

The qualitative and quantitative information about the impurities present in the electrolytes was obtained by ICP-OES (iCAP 7000) analysis. Of the elements analyzed such as Na, Mg, Al, Si, K, Ca, Cr, Fe, Co, Ni, Cu, Zn, Pt, and Pb, those excepted shown in Table 1 were not detected or present in trace amounts in tap water. To investigate the detrimental factors involving the impurities in tap water, stock solutions containing various combinations of metal ions were prepared using deionized water. The stock solution was *in situ* injected into electrolyte while observing the CO_2RR performance. The concentration of the stock solutions was 20 times higher than the target values listed in Table S2 in order to simulate the intended

impurity-environment by injecting a small amount of the solution without any undesirable effects. The list of stock solutions prepared was as follows: i) a solution for simulated tap water environment, containing group i (Ca, Na, and Mg) and group ii (Cu, Fe, and Zn) elements having concentrations listed in Table S2, ii) a solution containing only the group i impurities with the same concentration as that of solution i), iii) a solution containing only the group ii impurities with the same concentration as that of solution i), iv-vi) three solutions containing Cu, Fe, and Zn of the same concentration as that of solution iii), and vii-viii) two solutions of 20-fold (1 ppm of Cu, Fe, and Zn) and 200-fold (10 ppm of Cu, Fe, and Zn) concentrations compared to solution i). Various metal chlorides were selected as metal precursors for the stock solution except Na, because the tap water service in Seoul is chlorinated for sterilization. Therefore, deionized water containing only the Cl^- ion with the same concentrations as that of solution i) was also prepared to confirm the influence of Cl^-. The precursors used for preparing the stock solutions were $CaCl_2$ (≥97%, Sigma-Aldrich), $NaHCO_3$ (≥99.7%, Sigma-Aldrich), $MgCl_2$ (≥98%, Sigma), $FeCl_2$ (98%, Aldrich), $ZnCl_2$ (≥98%, Aldrich), $CuCl_2 \cdot 2H_2O$ (99.999%, Aldrich), and KCl (≥99.0%, Sigma-Aldrich).

2.5 Computational details.

We performed spin-polarized Density functional theory (DFT) calculations using the Vienna Ab-initio Simulation Package (VASP)[44] for the investigation of Fe adsorption energies on the four different Ag surfaces. We employed exchange-correlation functional of Perdew-Burke-Emzerhof[45] and the projector augmented wave (PAW) method.[46] And a plane-wave energy cutoff of 450 eV was used. Monkhorst k-point grids of (18×18×1) was employed for the optimization of the Ag bulk and the optimized bulk lattice parameter of a=4.15 Å for Ag is in good agreement with the experimental value of a=4.07 Å.[47] We built four different Ag slab models ([111], [100], [110], [331]) from the optimized Ag bulk structure by including an additional vacuum region of 20 Å. Gamma centered k-point grids of

(5×5×1), (7×7×1), (7×5×1) and (6×5×1) were employed for the Ag(111), Ag(100), Ag(110), and Ag(331) slab models, respectively. For all slab model calculations, one bottom layer was fixed at the lattice point to approximate the bulk while the other layers were allowed to relax, and the dipole correction was applied to the surface normal direction. For the calculation of Fe adsorption energy, we considered all possible adsorption sites on the Ag surfaces and reported only the adsorption energy at the most stable adsorption site.

3. Results and discussion

3.1 Origin of the performance degradation of metal-based catalyst in real water matrix.

To investigate the possible accompanied phenomenon during CO_2 reduction on a metal catalyst in practical condition, a Ag foil was used as a representative catalyst for CO production reaction. Note that Ag was selected as a standard catalyst in this study because of its remarkable intrinsic activity and reasonable material price compared to those of other candidates such as Au[10-13] and Pd[20]. The Ag foil exhibited a stable activity over 1 h with a CO Faradaic efficiency of 75% in a general electrolyte comprising CO_2-bubbled 0.5 M $KHCO_3$ using deionized water (Fig. 2a). In contrast, in the electrolyte containing unpurified tap water instead of deionized water, CO Faradaic efficiency rapidly decreased to *ca.* 20% within 30 min (Fig. 2b). This severe degradation led us to believe that Ag is highly vulnerable to impurities in water media, implying the limitation of metal-based catalysts for practical application. To identify the kinds and amount of impurities in tap water, its composition was investigated by inductively coupled plasma optical emission spectroscopy (ICP-OES) (Table 1). Impurities such as K, Ca, Na, Mg, Al, Cu, Fe, Zn, and Si were present in the tap water (service from Seoul, Korea).[48] We presume the effects of metal impurities can vary

depending on their ionized states and standard reduction potential relative to a given CO_2RR condition. Thus, the major impurities in tap water were classified into three groups: i) impurities remaining as cations in the electrolyte during the CO_2RR due to the extremely negative reduction potential (*i.e.*, K, Ca, Na, and Mg), ii) impurities that can be deposited on the electrode during the CO_2RR (*i.e.*, Cu, Fe, and Zn), and iii) impurities remaining as anions (*i.e.*, Al) or in the non-ionized state (*i.e.*, Si) under neutral conditions.

To evaluate the main contributors to catalyst deactivation in tap water, a stock solution simulating the tap water was prepared. Notably, Al and Si, which were assigned as group iii impurities, and K, which was already abundant in the electrolyte, could be excluded from consideration because CO_2RR is performed in a neutral electrolyte (0.5 M $KHCO_3$). Consequently, the stock solution containing Ca, Na, Mg, Cu, Fe, and Zn with an almost identical concentration to that of tap water was first applied (Table S2). During CO_2RR on the Ag electrode, a calculated amount of the stock solution was injected into the electrolyte and the *in situ* performance change was monitored. The performance of Ag decreased as soon as the stock solution was injected, which was very similar to that observed in the case of the real tap water electrolyte (Fig. 2c). Instead of *in situ* injection of the stock solution in the middle of CO_2RR, the catalytic performance of Ag electrode in the prepared simulated tap water was also monitored, showing the closer deactivation rate compared with that of Ag electrode in the real tap water condition (Fig. S2). This experiment supports the effect of metal impurities on the deactivation of the Ag electrode. Other components like organic species and mineral salts contained in real tap water, which were not included in a stock solution simulating tap water, cannot be excluded from possible deactivation factors for the Ag electrode. Nevertheless, a similar deactivation trend observed in

simulated tap water suggests that the main deactivation factors for the Ag electrode are among the components that we considered. A control *in situ* experiment verified that this phenomenon was not due to the presence of anions (*i.e.,* Cl^-) in the stock solution (Fig. 2d). Therefore, to determine the critical factors among the deliberately inserted impurities, two types of stock solutions were prepared containing either group i (*i.e.,* Ca, Na, and Mg) or group ii (*i.e.,* Cu, Fe, and Zn). Interestingly, no significant degradation in the catalytic activity was observed after the addition of the stock solution of group i (Fig. 2e), implying that alkali/alkali earth cations in tap water were not harmful impurities on Ag. It has been reported that cations could affect CO_2RR i) by adsorption at the cathode surface and stabilization of anions (*e.g.,* CO_2 reduction intermediate) in the electrical double layer region,[49] and ii) owing to the influence of the pH in the vicinity of the cathode by hydrolysis.[50] In fact, because divalent cations were even predicted to have a better effect towards CO_2RR than monovalent cations, the above experimental result does not deviate from the previous expectation.[50] However, it was also reported that the adlayer of cations and anions formed at the surface by ion-pairing might collapse the structure of the catalyst during the long-term reaction; therefore, it should be considered while investigating the stability when its concentration is high enough in electrolyte.[8,12]

Meanwhile, the stock solution of group ii revealed a significant deactivation (Fig. 2f), similar to that observed with the stock solution simulating tap water (Fig. 2c). This could be strong evidence that the prime candidates responsible for deactivations are Cu, Fe, or Zn which can deposit onto the surface. Hence, it can be proposed that the CO_2RR electrocatalyst is deteriorated not by the presence of metal ions in the electrolyte but by the deposition of the impurity metal on the catalyst surface. Indeed, after the CO_2RR in tap water, the deposition of Cu, Fe, and Zn on the Ag surface was

verified by XPS (Fig. S3). The accumulation of carbon on the surface, which is known to be one of the reasons for catalyst deactivation in the CO_2RR system, was also detected (Fig. S4). However, similar carbon signals were obtained on the Ag electrode surfaces after CO_2RR in deionized water and tap water (Fig. S4b and c).[12] Considering the rapid performance degradation in tap water and the relatively stable performance in deionized water over the same period, carbon deposition on the Ag electrode surface could not be considered a critical factor for fast deactivation in low-purity water. To further unearth the most detrimental impurities in the solution that have not yet been determined, stock solutions containing Cu, Fe, and Zn each were prepared again, and their effects were investigated. Fe explosively accelerated H_2 evolution (HER) at the Ag electrode, while Cu and Zn slightly decreased the current density and CO Faradaic efficiency (Fig. 2g-i and Fig. S5). To study the effect of metal impurity, stock solutions containing different Fe concentrations (*i.e.*, 0.025, 0.05, and 0.1 ppm) were respectively injected into the electrolytes, and proportional performance degradation due to increased Fe concentration was observed, verifying that the Fe impurity metal affects the deactivation process on the Ag foil (Fig. S6).

Although it has been suggested that impurity metal deposition is one of the reasons, it has not yet been clarified how very low concentrations of metal ions have significant effects on performance degradation. To solve this problem, we assumed that the metal deposition was different depending on the surface energy.[46] X-ray diffraction (XRD) analysis revealed that the polycrystalline Ag foil used herein was composed of four main different planes, viz. (111), (200), (220), and (311) (Fig. S7). The surface free energies of these planes were in the order of $\gamma_{(111)} < \gamma_{(100)} < \gamma_{(110)} < \gamma_{(311)}$, suggesting different affinity toward impurity deposition along each plane.[47] DFT calculation was conducted to obtain Fe adsorption energy as a representative value.

Each Ag surface exhibits different adsorption energies toward the Fe metal, suggesting that the Fe adsorption rates depended on the Ag planes (Fig. 3). Unfortunately, these easily contaminated planes show high reactivities toward CO_2-to-CO conversion according to previously reported DFT calculation results.[48] In other words, since the contamination by metal impurity preferentially initiates from the highly active planes, it causes significant deactivation despite low concentration of impurity. Therefore, use of the surface-energy-modified metal-based catalyst, *e.g.*, plane-controlled structure, might be the one of the strategies to mitigate the deactivation by metal impurities.

3.2 Design strategy for durable catalyst in real water matrix.

Based on the fruitful studies involving Ag, we established our strategy for designing a highly stable catalyst in tap water; the catalyst should be free from the effect of metal impurity deposition and/or carbon deposition. This led us to consider a metal-free carbon-based catalyst as a reasonable candidate because of the expected intrinsic resistance to carbon deposition and more importantly, feature of non-metallic active sites that are insensitive to impurity metals. In addition, heteroatom-doping in carbon-based materials have been demonstrated to be effective to increasing the CO_2RR activity.[36-43] Although the heteroatom-doped carbon-based catalyst still suffers from a lack of understanding with regard to the nature of the active sites, many researchers have proposed that the catalyst has an electrochemical ability to reduce CO_2 without any metal inclusion;[36-43] therefore, it appeared to be an appropriate material for our design strategy. Thus, CNTs, selected as raw material due to high conductivity and good flexibility of morphology control, having active sites of doped N atoms were chosen as a model catalyst for our study. The catalyst was simply prepared by ball milling of CNT and acid treatment using HNO_3 followed by N-doping with only dicyandiamide (Fig. 4a and b). The ball milling process was

conducted for introducing high defect density and enlarged surface area by obtaining short CNTs. Acid treatment was further performed to introduce various oxygen functional groups on the surface for facile N-doping. To cross-correlate the effects of each procedure with physical properties, two additional N-doped CNT catalysts were synthesized: i) N-oxi-CNT prepared by acid treatment and N-doping processes of CNT and ii) N-CNT prepared by only N-doping (Fig. 4a). TEM directly revealed the relatively short morphology of ball mill N-CNT, having discontinuous edges compared to N-oxi-CNT and N-CNT, as expected (Fig. 4c and Fig. S8). The amount of the N dopant was observed to gradually increase from 0.18 to 1.66 at.% in the order of N-CNT, N-oxi-CNT, and ball mill N-CNT (Table S3), and the same trend was observed in the Raman spectra (Fig. 4d), which showed the degree of defect sites in carbon-based materials in terms of the I_D/I_G ratio (I_D is the D band intensity at 1,350 cm^{-1} derived from the breathing modes of the sp^2-hybridized ring and requires a defect for its activation, and I_G is the G band intensity at 1,589 cm^{-1} corresponding to the doubly degenerate E_{2g} phonon at the Brillouin-zone center);[51] these findings further support the effect of both ball milling and acid treatment. Additionally, the chemical nature of doped N in ball mill N-CNT was analyzed using an XPS−N_{1s} spectrum (Fig. S9), and the compositions were calculated based on the results of elemental analysis: 0.90% of pyridinic N (398.2 eV), 0.48% of pyrrolic N (399.9 eV), 0.21% graphitic N (401.2 eV), and 0.07% oxidized N (403.0 eV) (Fig. 4e).

To diagnose the overall performance of the prepared catalysts, the electrochemical CO_2RR was carried out at various applied potentials in a CO_2-bubbled 0.5 M $KHCO_3$ electrolyte using deionized water. These data were obtained by performing step-potential electrolysis with periodic quantification of the gaseous products by gas chromatography (GC). The products from CO_2 electrolysis were CO and H_2 with the

net total Faradaic efficiency nearly 100%. Among them, ball mill N-CNT exhibited the best performance in terms of CO Faradaic efficiency and current density: the highest CO Faradaic efficiency of 73% with −3 mA cm^{-2} of current density at −0.46 V_{RHE}, which was 14% and 52% higher than those of N-oxi-CNT and N-CNT, respectively (Fig. 5a). We confirmed that the carbon source of the produced CO was not the carbon catalyst itself, but CO_2 by observing the rapidly changing catalytic performance of ball mill N-CNT depending on the type of supplied gas, inert gas (He) and CO_2 (Fig. S10). Compared to the catalytic activity of the Ag foil, the ball mill N-CNT exhibited a comparable value of the maximum CO Faradaic efficiency at lower overpotentials without metal-based active sites. It could be deduced that the ball mill N-CNT contains doped N-based active sites based on the nearly linear correlation between the N content and the CO production of the prepared catalysts (Fig. S11), leading us to expect a successful operation of ball mill N-CNT as a CO_2RR catalyst. Notably, the performance of ball mill N-CNT was not affected by *in situ* injection of the stock solution used for simulating tap water unlike the case of Ag (Fig. 5b) and more importantly, there was little difference in the performance of ball mill N-CNT between the two electrolytes using deionized water and real tap water (Fig. 5c). To directly compare the behaviour of impurity deposition depending on the electrodes, CO_2RRs on both electrodes (*i.e.*, Ag foil and ball mill N-CNT) were performed at the same applied potential of −1.0 V_{RHE}, and then the post-reaction surfaces were analysed by XPS (Fig. S12). On the surface of ball mill N-CNT, the impurity metal deposition was not observed in contrast to the Cu, Fe, and Zn deposition identified in the aforementioned Ag case. Thus, this indicated that the intrinsic surface property of catalyst was important to determine the metal deposition preference during CO_2RR, which might be contributed to the improvement of durability of ball mill N-CNT.

3.3 Stable operation in real water matrix.

To determine the potential of ball mill N-CNT as a catalyst for practical application, its long-term stabilities in the tap water electrolyte (Fig. 5e) as well as in deionized water (Fig. 5d) were tested. The long-term operations were performed through sequentially programmed cycles involving an applied constant potential, which was selected as the potential showing the highest Faradaic efficiency for CO production, and a short period of the resting step (open cell) to facilitate the transport of trapped products on porous carbon. The ball mill N-CNT showed a stable performance during its unprecedented long-term operation for 120 h even in tap water: the CO Faradaic efficiency was preserved as *ca.* 70% with −3 mA cm^{-2} of the current density. Interestingly, despite the excellent durability of ball mill N-CNT in practical conditions, irregular deposition of single and/or small particle-shaped metals composed of Cu, Fe, and/or Zn, and Pt (Pt ions might be migrated through dissolution of Pt counter electrode during the long-term operation.[8,52]) was observed on the surface of a post-reaction sample by high-angle annular dark-field (HAADF) images of STEM, EDX, and X-ray analyses (Fig. 6a-e and Fig. S13). This implied that the active sites of ball mill N-CNT are still alive despite impurity metal deposition. Impurity metal ions preferentially deposit on nucleophilic sites such as i) carbon defects and ii) N-doped sites;[53] it was cautiously expected that either case barely hinders the CO_2RR performance of ball mill N-CNT. First, the carbon defects are independent of the anticipated active sites of CO_2RR in N-CNT catalysts. In the second case, even if the metals bind with the N-species, they might not significantly decrease the CO_2RR performance because metal binding with N could serve as active sites for CO_2RR, *i.e.*, metal-N_x-C (*e.g.*, Fe-N-C).[53,54] To investigate the structural change due to metal deposition, especially that of the state of Fe, which can be

considered a major element deposited on ball mill N-CNT, Fe *K*-edge *ex situ* XANES spectra were analyzed (Fig. S13d). In the Fe *K*-edge spectrum, Fe was significantly deposited on the abundant carbon defects in ball mill N-CNT and was naturally oxidized by exposure to air after the reaction because Fe was close to its natural oxidized state of Fe^{3+}. These Fe deposits may act as active sites for independent HER even if they were deposited on carbon defects, but resultingly, they did not have a significant impact (Fig. S14); it was supposed that Fe particle did not enough to be formed which can act proper active site for HER on ball mill N-CNT. Furthermore, ball mill N-CNT exhibited remarkable tolerance to harsh condition, where 20-fold to 200-fold higher concentrations of Cu, Fe, and Zn impurities compared to tap water were permitted (Fig. 6f and g). These demonstrated that ball mill N-CNT have the strong resistant potential against the impurities because the influence of impurity metals on N-doped CNTs was different from that on metal-based catalyst.

Since this property of ball mill N-CNT might be attributed to durable active sites, the N species, which were associated with the CO_2-to-CO conversion activity (Fig. S11), of the as-prepared and post-reaction samples were examined by XPS analysis. Although it is still controversial whether the local sites derived from N-doping process, such as pyridinic N, pyrrolic N, graphitN, and carbon adjacent to N, are the active sites for CO_2RR, pyridinic N is generally considered one of the most valid active sites.[36,41,55] Similarly, the changed nature of N in ball mill N-CNT after CO_2RR seems to indicate the involvement of N in CO_2RR (Fig. S15); the relative concentration of pyridinic N was decreased from 54% to 30% while that of pyrrolic N increased from 29% to 50%. According to previous reports, this phenomenon was interpreted to be due to the CO_2 adsorbed on pyridinic N; consequently, pyridinic N operated as the active site for CO_2RR.[41-43] Nevertheless, none of these is a direct

evidence to prove the active site for CO_2RR; therefore, we still consider other possibilities regarding the active site for our catalyst.

4. Conclusions

In conclusion, the origin of the performance deactivation of Ag in real water matrix, tap water, was investigated by experimental screening of the phenomenon under various simulated conditions. Among the various components of tap water, the critical factor that affects performance degradation was not the impurities remaining as cations in the electrolyte, but the impurities depositing on the surface such as Cu, Zn, and especially Fe. This result suggested that the design strategy for a stable catalyst in future applied practical conditions would be protection of active sites from detrimental factors or the development of tolerant active sites for those factors. Following the latter strategy, a modified N-doped CNT catalyst was developed herein as a stable catalyst with non-metal-based active sites such as N-C sites. Consequently, the CO_2 reduction performance of ball mill N-CNT was maintained in tap water electrolyte during 120 h long-term operations with 70% of CO Faradaic efficiency and −3 mA cm^{-2} of current density and even in more harsh environments. We believe that this work can be a guide towards achieving practical application of a highly durable catalyst for the CO_2RR, whose feasibility in the presence of detrimental impurities unavoidably present in realistic water conditions was demonstrated by a simple catalyst design strategy.

Acknowledgements

This work was supported by the program of the Korea Institute of Science and Technology (KIST) and partially by “Next Generation Carbon Upcycling Project” (Project No.

2017M1A2A2046713) through the National Research Foundation (NRF) funded by the Korean government.

Conflict of interest The authors declare no competing financial interests.

References

[1] G.A. Olah, G.K.S. Prakash, A. Goeppert, Anthropogenic Chemical Carbon Cycle for a Sustainable Future, J. Am. Chem. Soc., 133 (2011) 12881-12898. https://doi.org/10.1021/ja202642y.

[2] J. Qiao, Y. Liu, F. Hong, J. Zhang, A review of catalysts for the electroreduction of carbon dioxide to produce low-carbon fuels, Chem. Soc. Rev., 43 (2014) 631-675. https://doi.org/10.1039/C3CS60323G.

[3] C. Costentin, M. Robert, J.M. Savéant, Catalysis of the electrochemical reduction of carbon dioxide, Chem. Soc. Rev., 42 (2013) 2423-2436. https://doi.org/10.1039/c2cs35360a.

[4] Y. Yoon, A.S. Hall, Y. Surendranath, Tuning of Silver Catalyst Mesostructure Promotes Selective Carbon Dioxide Conversion into Fuels, Angew. Chem. Int. Ed., 55 (2016) 15282-15286. https://doi.org/10.1002/anie.201607942.

[5] Q. Lu, J. Rosen, Y. Zhou, G.S. Hutchings, Y.C. Kimmel, J.G. Chen, F. Jiao, A selective and efficient electrocatalyst for carbon dioxide reduction, Nat. Commun., 5 (2014) 3242-3247. https://doi.org/10.1038/ncomms4242.

[6] C. Kim, H.S. Jeon, T. Eom, M.S. Jee, H. Kim, C.M. Friend, B.K. Min, Y.J. Hwang, Achieving Selective and Efficient Electrocatalytic Activity for CO_2 Reduction Using Immobilized Silver Nanoparticles, J. Am. Chem. Soc., 137 (2015) 13844-13850. https://doi.org/10.1021/jacs.5b06568.

[7] S. Liu, H. Tao, L. Zeng, Q. Liu, Z. Xu, Q. Liu, J.-L. Luo, Shape-Dependent Electrocatalytic Reduction of CO_2 to CO on Triangular Silver Nanoplates, J. Am. Chem. Soc., 139 (2017) 2160-2163. https://doi.org/10.1021/jacs.6b12103.

[8] Y.-C. Hsieh, S.D. Senanayake, Y. Zhang, W. Xu, D.E. Polyansky, Effect of Chloride Anions on the Synthesis and Enhanced Catalytic Activity of Silver Nanocoral Electrodes for CO_2 Electroreduction, ACS Catal., 5 (2015) 5349-5356.

https://doi.org/10.1021/acscatal.5b01235.

[9] M. Ma, B.J. Trześniewski, J. Xie, W.A. Smith, Selective and Efficient Reduction of Carbon Dioxide to Carbon Monoxide on Oxide-Derived Nanostructured Silver Electrocatalysts, Angew. Chem. Int. Ed., 55 (2016) 9748-9752. https://doi.org/10.1002/anie.201604654.

[10] M. Liu, Y. Pang, B. Zhang, P. De Luna, O. Voznyy, J. Xu, X. Zheng, C.T. Dinh, F. Fan, C. Cao, F.P.G. de Arquer, T.S. Safaei, A. Mepham, A. Klinkova, E. Kumacheva, T. Filleter, D. Sinton, S.O. Kelley, E.H. Sargent, Enhanced electrocatalytic CO_2 reduction via field-induced reagent concentration, Nature, 537 (2016) 382-386. https://doi.org/10.1038/nature19060.

[11] W. Zhu, Y.-J. Zhang, H. Zhang, H. Lv, Q. Li, R. Michalsky, A.A. Peterson, S. Sun, Active and Selective Conversion of CO_2 to CO on Ultrathin Au Nanowires, J. Am. Chem. Soc., 136 (2014) 16132-16135. https://doi.org/10.1021/ja5095099.

[12] H. Kim, H.S. Jeon, M.S. Jee, E.B. Nursanto, J.P. Singh, K. Chae, Y.J. Hwang, B.K. Min, Contributors to Enhanced CO_2 Electroreduction Activity and Stability in a Nanostructured Au Electrocatalyst, ChemSusChem, 9 (2016) 2097-2102. https://doi.org/10.1002/cssc.201600228.

[13] R.G. Mariano, K. McKelvey, H.S. White, M.W. Kanan, Selective increase in CO_2 electroreduction activity at grain-boundary surface terminations, Science, 358 (2017) 1187-1192. https://doi.org/10.1126/science.aao3691.

[14] H. Mistry, A.S. Varela, C.S. Bonifacio, I. Zegkinoglou, I. Sinev, Y.-W. Choi, K. Kisslinger, E.A. Stach, J.C. Yang, P. Strasser, B.R. Cuenya, Highly selective plasma-activated copper catalysts for carbon dioxide reduction to ethylene, Nat. Commun., 7 (2016) 12123-12130. https://doi.org/10.1038/ncomms12123.

[15] F.S. Roberts, K.P. Kuhl, A. Nilsson, High Selectivity for Ethylene from Carbon Dioxide Reduction over Copper Nanocube Electrocatalysts, Angew. Chem. Int. Ed., 54 (2015) 5179-5182. https://doi.org/10.1002/anie.201412214.

[16] P. De Luna, R. Quintero-Bermudez, C.-T. Dinh, M.B. Ross, O.S. Bushuyev, P. Todorović, T. Regier, S.O. Kelley, P. Yang, E.H. Sargent, Catalyst electro-redeposition controls morphology and oxidation state for selective carbon dioxide reduction, Nat. Catal., 1 (2018) 103-110. https://doi.org/10.1038/s41929-017-0018-9.

[17] D.H. Won, C.H. Choi, J. Chung, M.W. Chung, E.-H. Kim, S.I. Woo, Rational Design of a Hierarchical Tin Dendrite Electrode for Efficient Electrochemical Reduction of CO_2, ChemSusChem, 8 (2015) 3092-3098. https://doi.org/10.1002/cssc.201500694.

[18] S. Zhang, P. Kang, T.J. Meyer, Nanostructured Tin Catalysts for Selective Electrochemical Reduction of Carbon Dioxide to Formate, J. Am. Chem. Soc., 136 (2014) 1734-1737. https://doi.org/10.1021/ja4113885.

[19] F. Lei, W. Liu, Y. Sun, J. Xu, K. Liu, L. Liang, T. Yao, B. Pan, S. Wei, Y. Xie, Metallic tin quantum sheets confined in graphene toward high-efficiency carbon dioxide electroreduction, Nat. Commun., 7 (2016) 12697-12704. https://doi.org/10.1038/ncomms12697.

[20] D. Gao, H. Zhou, J. Wang, S. Miao, F. Yang, G. Wang, J. Wang, X. Bao, Size-Dependent Electrocatalytic Reduction of CO_2 over Pd Nanoparticles, J. Am. Chem. Soc., 137 (2015) 4288-4291. https://doi.org/10.1021/jacs.5b00046.

[21] X. Min, M.W. Kanan, Pd-Catalyzed Electrohydrogenation of Carbon Dioxide to Formate: High Mass Activity at Low Overpotential and Identification of the Deactivation Pathway, J. Am. Chem. Soc., 137 (2015) 4701-4708. https://doi.org/10.1021/ja511890h.

[22] D.H. Won, H. Shin, J. Koh, J. Chung, H.S. Lee, H. Kim, S.I. Woo, Highly Efficient, Selective, and Stable CO_2 Electroreduction on a Hexagonal Zn Catalyst, Angew. Chem. Int. Ed., 55 (2016) 9297-9300. https://doi.org/10.1002/anie.201602888.

[23] J. Rosen, G.S. Hutchings, Q. Lu, R.V. Forest, A. Moore, F. Jiao, Electrodeposited Zn Dendrites with Enhanced CO Selectivity for Electrocatalytic CO_2 Reduction, ACS Catal., 5

(2015) 4586-4591. https://doi.org/10.1021/acscatal.5b00922.

[24] J.H. Koh, D.H. Won, T. Eom, N.-K. Kim, K.D. Jung, H. Kim, Y.J. Hwang, B.K. Min, Facile CO_2 Electro-Reduction to Formate via Oxygen Bidentate Intermediate Stabilized by High-Index Planes of Bi Dendrite Catalyst, ACS Catal., 7 (2017) 5071-5077. https://doi.org/10.1021/acscatal.7b00707.

[25] F. Yang, P. Song, X. Liu, B. Mei, W. Xing, Z. Jiang, L. Gu, W. Xu, Highly Efficient CO_2 Electroreduction on ZnN_4-based Single-Atom Catalyst, Angew. Chem. Int. Ed., (2018). https://doi.org/10.1002/anie.201805871.

[26] C. Zhao, X. Dai, T. Yao, W. Chen, X. Wang, J. Wang, J. Yang, S. Wei, Y. Wu, Y. Li, Ionic Exchange of Metal–Organic Frameworks to Access Single Nickel Sites for Efficient Electroreduction of CO_2, J. Am. Chem. Soc., 139 (2017) 8078-8081. https://doi.org/10.1021/jacs.7b02736.

[27] X. Wang, Z. Chen, X. Zhao, T. Yao, W. Chen, R. You, C. Zhao, G. Wu, J. Wang, W. Huang, J. Yang, X. Hong, S. Wei, Y. Wu, Y. Li, Regulation of Coordination Number over Single Co Sites: Triggering the Efficient Electroreduction of CO_2, Angew. Chem. Int. Ed., 57 (2018) 1944-1948. https://doi.org/10.1002/anie.201712451.

[28] H.B. Yang, S.-F. Hung, S. Liu, K. Yuan, S. Miao, L. Zhang, X. Huang, H.-Y. Wang, W. Cai, R. Chen, J. Gao, X. Yang, W. Chen, Y. Huang, H.M. Chen, C.M. Li, T. Zhang, B. Liu, Atomically dispersed Ni(i) as the active site for electrochemical CO_2 reduction, Nat. Energy, 3 (2018) 140-147. https://doi.org/10.1038/s41560-017-0078-8.

[29] Y. Hori, H. Konishi, T. Futamura, A. Murata, O. Koga, H. Sakurai, K. Oguma, "Deactivation of copper electrode" in electrochemical reduction of CO_2, Electrochim. Acta, 50 (2005) 5354-5369. https://doi.org/10.1016/j.electacta.2005.03.015.

[30] B. Kumar, J.P. Brian, V. Atla, S. Kumari, K.A. Bertram, R.T. White, J.M. Spurgeon, New trends in the development of heterogeneous catalysts for electrochemical CO_2 reduction,

Catal. Today, 270 (2016) 19-30. https://doi.org/10.1016/j.cattod.2016.02.006.

[31] A. Wuttig, Y. Surendranath, Impurity Ion Complexation Enhances Carbon Dioxide Reduction Catalysis, ACS Catal., 5 (2015) 4479-4484. https://doi.org/10.1021/acscatal.5b00808.

[32] Ministry of Environment, Republic of Korea, Management Criteria 'Soil and Groundwater', 2013.

[33] A.d. Klerk, Fischer-Tropsch fuels refinery design, Energy Environ. Sci., 4 (2011) 1177-1205. https://doi.org/10.1039/C0EE00692K.

[34] P. Hermange, A.T. Lindhardt, R.H. Taaning, K. Bjerglund, D. Lupp, T. Skrydstrup, Ex Situ Generation of Stoichiometric and Substoichiometric ^{12}CO and ^{13}CO and Its Efficient Incorporation in Palladium Catalyzed Aminocarbonylations, J. Am. Chem. Soc., 133 (2011) 6061-6071. https://doi.org/10.1021/ja200818w.

[35] A. Sen, Catalytic Synthesis of Alkene-Carbon Monoxide Copolymers and Cooligomers, Springer, Boston, 2003.

[36] J. Wu, R.M. Yadav, M. Liu, P.P. Sharma, C.S. Tiwary, L. Ma, X. Zou, X.-D. Zhou, B.I. Yakobson, J. Lou, P.M. Ajayan, Achieving Highly Efficient, Selective, and Stable CO_2 Reduction on Nitrogen-Doped Carbon Nanotubes, ACS Nano, 9 (2015) 5364-5371. https://doi.org/10.1021/acsnano.5b01079.

[37] X. Cui, Z. Pan, L. Zhang, H. Peng, G. Zheng, Selective Etching of Nitrogen-Doped Carbon by Steam for Enhanced Electrochemical CO_2 Reduction, Adv. Energy Mater., 7 (2017) 1701456-1701461. https://doi.org/10.1002/aenm.201701456.

[38] P.P. Sharma, J. Wu, R.M. Yadav, M. Liu, C.J. Wright, C.S. Tiwary, B.I. Yakobson, J. Lou, P.M. Ajayan, X.-D. Zhou, Nitrogen-Doped Carbon Nanotube Arrays for High-Efficiency Electrochemical Reduction of CO_2: On the Understanding of Defects, Defect Density, and Selectivity, Angew. Chem., 127 (2015) 13905-13909.

https://doi.org/10.1002/ange.201506062.

[39] H.-R.M. Jhong, C.E. Tornow, B. Smid, A.A. Gewirth, S.M. Lyth, P.J.A. Kenis, A Nitrogen-Doped Carbon Catalyst for Electrochemical CO_2 Conversion to CO with High Selectivity and Current Density, ChemSusChem, 10 (2017) 1094-1099. https://doi.org/10.1002/cssc.201600843.

[40] J. Xu, Y. Kan, R. Huang, B. Zhang, B. Wang, K.H. Wu, Y. Lin, X. Sun, Q. Li, G. Centi, D. Su, Revealing the Origin of Activity in Nitrogen-Doped Nanocarbons towards Electrocatalytic Reduction of Carbon Dioxide, ChemSusChem, 9 (2016) 1085-1089. https://doi.org/10.1002/cssc.201600202.

[41] J. Wu, S. Ma, J. Sun, J.I. Gold, C. Tiwary, B. Kim, L. Zhu, N. Chopra, I.N. Odeh, R. Vajtai, A.Z. Yu, R. Luo, J. Lou, G. Ding, P.J.A. Kenis, P.M. Ajayan, A metal-free electrocatalyst for carbon dioxide reduction to multi-carbon hydrocarbons and oxygenates, Nat. Commun., 7 (2016) 13869-13874. https://doi.org/10.1038/ncomms13869.

[42] J. Wu, M. Liu, P.P. Sharma, R.M. Yadav, L. Ma, Y. Yang, X. Zou, X.-D. Zhou, R. Vajtai, B.I. Yakobson, J. Lou, P.M. Ajayan, Incorporation of Nitrogen Defects for Efficient Reduction of CO_2 via Two-Electron Pathway on Three-Dimensional Graphene Foam, Nano Letters, 16 (2016) 466-470. https://doi.org/10.1021/acs.nanolett.5b04123.

[43] B. Kumar, M. Asadi, D. Pisasale, S. Sinha-Ray, B.A. Rosen, R. Haasch, J. Abiade, A.L. Yarin, A. Salehi-Khojin, Renewable and metal-free carbon nanofibre catalysts for carbon dioxide reduction, Nat. Commun., 4 (2013) 2819-2826. 10.1038/ncomms3819.

[44] G. Kresse, J. Furthmüller, Efficient iterative schemes for ab initio total-energy calculations using a plane-wave basis set, Phys .Rev. B, 54 (1996) 11169-11186. https://doi.org/10.1103/PhysRevB.54.11169.

[45] J.P. Perdew, K. Burke, M. Ernzerhof, Generalized Gradient Approximation Made Simple, Phys. Rev. Lett., 77 (1996) 3865-3868. https://doi.org/10.1103/PhysRevLett.77.3865.

[46] P.E. Blöchl, Projector augmented-wave method, Phys .Rev. B, 50 (1994) 17953-17979. https://doi.org/10.1103/PhysRevB.50.17953.

[47] P. Haas, F. Tran, P. Blaha, Calculation of the lattice constant of solids with semilocal functionals, Phys .Rev. B, 79 (2009) 085104. https://doi.org/10.1103/PhysRevB.79.085104.

[48] Seoul Metropolitan Government, Republic of Korea, Seoul Tap Water Arisu, 2014.

[49] M.R. Thorson, K.I. Siil, P.J.A. Kenis, Effect of Cations on the Electrochemical Conversion of CO_2 to CO, J. Electrochem. Soc., 160 (2013) F69-F74. https://doi.org/10.1149/2.052301jes.

[50] M.R. Singh, Y. Kwon, Y. Lum, J.W. Ager, A.T. Bell, Hydrolysis of Electrolyte Cations Enhances the Electrochemical Reduction of CO_2 over Ag and Cu, J. Am. Chem. Soc., 138 (2016) 13006-13012. https://doi.org/10.1021/jacs.6b07612.

[51] T.M.G. Mohiuddin, A. Lombardo, R.R. Nair, A. Bonetti, G. Savini, R. Jalil, N. Bonini, D.M. Basko, C. Galiotis, N. Marzari, K.S. Novoselov, A.K. Geim, A.C. Ferrari, Uniaxial strain in graphene by Raman spectroscopy: ***G*** peak splitting, Gruneisen parameters, and sample orientation, Phys .Rev. B, 79 (2009) 205433. https://doi.org/10.1103/PhysRevB.79.205433.

[52] C. Gu, B.C. Norris, F.-R.F. Fan, C.W. Bielawski, A.J. Bard, Is Base-Inhibited Vapor Phase Polymerized PEDOT an Electrocatalyst for the Hydrogen Evolution Reaction? Exploring Substrate Effects, Including Pt Contaminated Au, ACS Catal., 2 (2012) 746-750. https://doi.org/10.1021/cs3000107.

[53] Y. Zhou, K. Neyerlin, T.S. Olson, S. Pylypenko, J. Bult, H.N. Dinh, T. Gennett, Z. Shao, R. O'Hayre, Enhancement of Pt and Pt-alloy fuel cell catalyst activity and durability via nitrogen-modified carbon supports, Energy Environ. Sci., 3 (2010) 1437-1446. https://doi.org/10.1039/C003710A.

[54] T.N. Huan, N. Ranjbar, G. Rousse, M. Sougrati, A. Zitolo, V. Mougel, F. Jaouen, M.

Fontecave, Electrochemical Reduction of CO_2 Catalyzed by Fe-N-C Materials: A Structure–Selectivity Study, ACS Catal., 7 (2017) 1520-1525. https://doi.org/10.1021/acscatal.6b03353.

[55] S. Siahrostami, K. Jiang, M. Karamad, K. Chan, H. Wang, J. Nørskov, Theoretical Investigations into Defected Graphene for Electrochemical Reduction of CO_2, ACS Sustainable Chem. Eng., 5 (2017) 11080-11085. https://doi.org/10.1021/acssuschemeng.7b03031.

Figure and Figure Captions

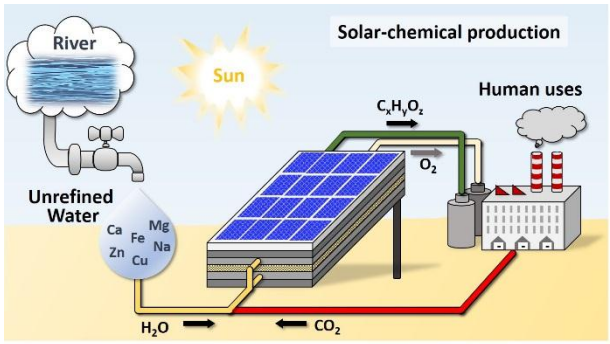

Fig. 1 Schematic description of a practical solar-chemical production system. Electrochemical conversion of CO_2 and water to value-added chemicals powered by sunlight. For massive production through large-scale system, a plausible condition is to utilize the practical or real-life used water as an industrial water.

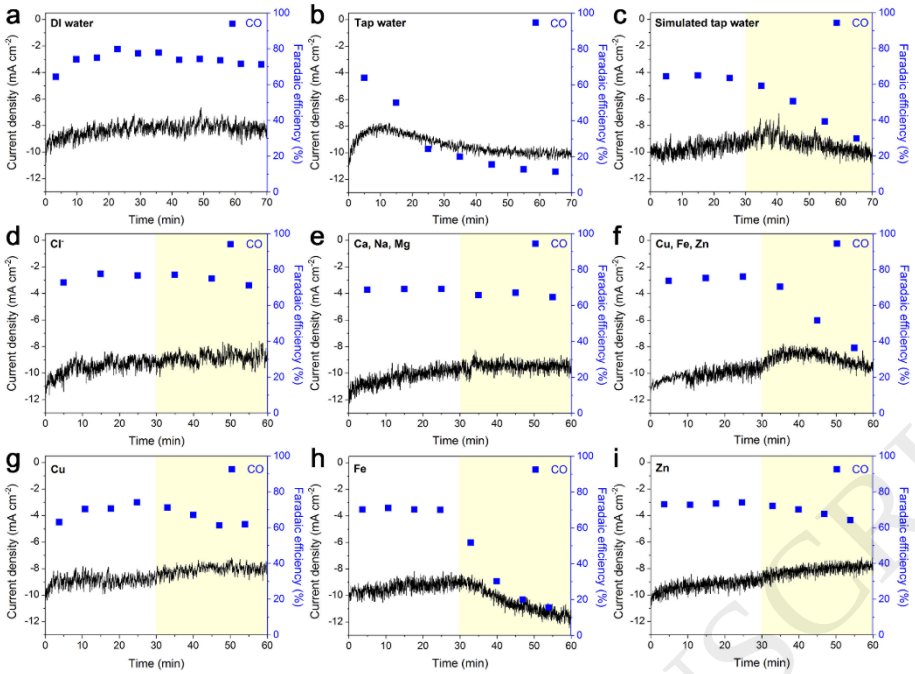

Fig. 2 Performance trends of a Ag electrode with respect to the electrolyte water conditions. CO_2 reduction activity in a CO_2-bubbled 0.5 M $KHCO_3$ electrolyte at −1.0 V (*vs.* RHE) using (a) deionized water and (b) tap water. The observed performance profile after *in situ* injection of various stock solutions in the CO_2-bubbled 0.5 M $KHCO_3$ electrolyte at −1.0 V (*vs.* RHE) using deionized water: (c) a solution for simulating the tap water environment, containing group i (*i.e.*, Ca, Na, and Mg) and group ii (*i.e.*, Cu, Fe, and Zn) elements, (d) a solution containing only Cl^- ions, (e) a solution containing group i impurities, (f) a solution containing group ii impurities, and three solutions containing (g) Cu, (h) Fe, and (i) Zn (the black line, blue square, and yellow background represent current density, CO Faradaic efficiency, and behaviour after the injection of stock solution, respectively.).

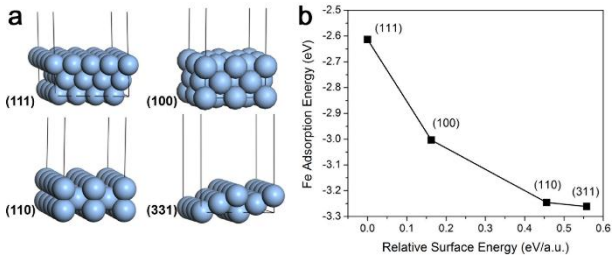

Fig. 3 DFT calculation of Fe adsorption on Ag surfaces. (a) The four different Ag slab models built from the optimized Ag bulk. (b) Fe adsorption energy as a function of relative surface energy of the four different Ag surfaces, viz. (111), (100), (110), and (311).

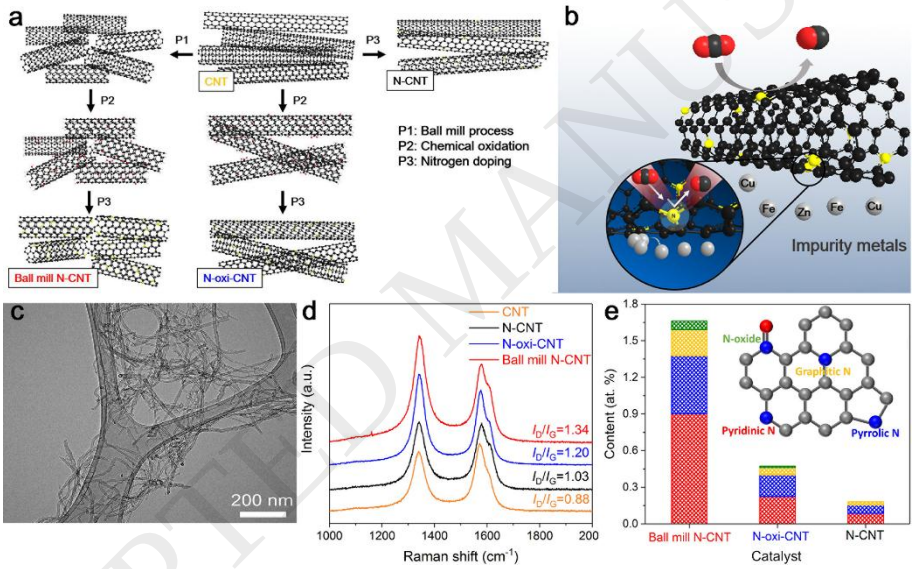

Fig. 4 Physical characterization of prepared CNT catalysts. (a) A scheme of synthesis processes of N-doped CNT catalysts, viz. N-CNT, N-oxi-CNT, and ball mill N-CNT (black, yellow, red, and white circles represent C, N, O, and H, respectively). (b) A scheme for the design strategy of ball mill N-CNT. (c) Morphology of ball mill N-CNT observed under TEM analysis. (d) Raman spectroscopy of the catalysts with I_D/I_G ratios of prepared CNT catalysts. (e) Atomic content of doped N calculated by combining XPS−N_{1s} and elemental analysis (inset: structural models of N atoms in N-doped carbon catalyst. Blue, gray and red colors represent N, C, and O atoms, respectively.).

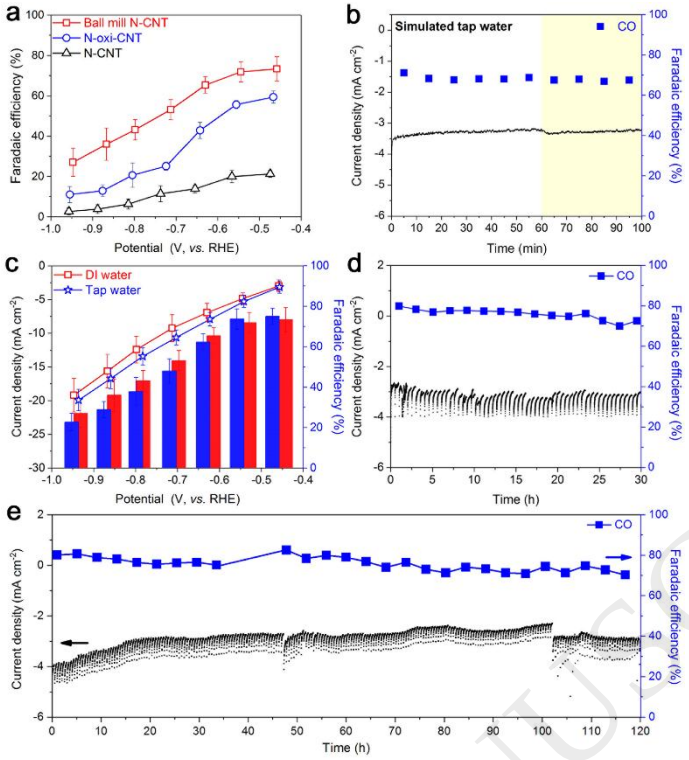

Fig. 5 Performance of the ball mill N-CNT catalyst on CO_2RR. (a) Catalytic activity of ball mill N-CNT compared to other prepared N-doped catalysts in terms of CO Faradaic efficiency in CO_2-bubbled 0.5 M $KHCO_3$ using deionized water in the potential range from −0.46 to −0.95 V (*vs.* RHE) (the black triangle, blue circle, and red square represent N-CNT, N-oxi-CNT, and ball mill N-CNT, respectively.). The durability of ball mill N-CNT towards metal impurities examined through (b) *in situ* injection of a solution for simulating the tap water in CO_2-bubbled 0.5 M $KHCO_3$ at −0.46 V (*vs.* RHE) (the black line, blue square, and yellow background represent the current density, CO Faradaic efficiency, and behaviour after the injection of stock solution, respectively.) and (c) performances observed in CO_2-bubbled 0.5 M $KHCO_3$ electrolytes using deionized (the red square and red bar represent current density and CO Faradaic efficiency, respectively.) and tap water (the blue star and blue bar represent current density and CO Faradaic efficiency, respectively.) at various applied potentials. Long-term operation of ball mill N-CNT in CO_2-bubbled 0.5 M $KHCO_3$ using (d) deionized water at −0.46 V (*vs.* RHE) and (e) tap water at −0.44 V (*vs.* RHE). The electrolyte

was supplemented twice when the CO_2 reduction reaction had elapsed 48 h and 102 h (the black line and blue square represent current density and CO Faradaic efficiency, respectively.).

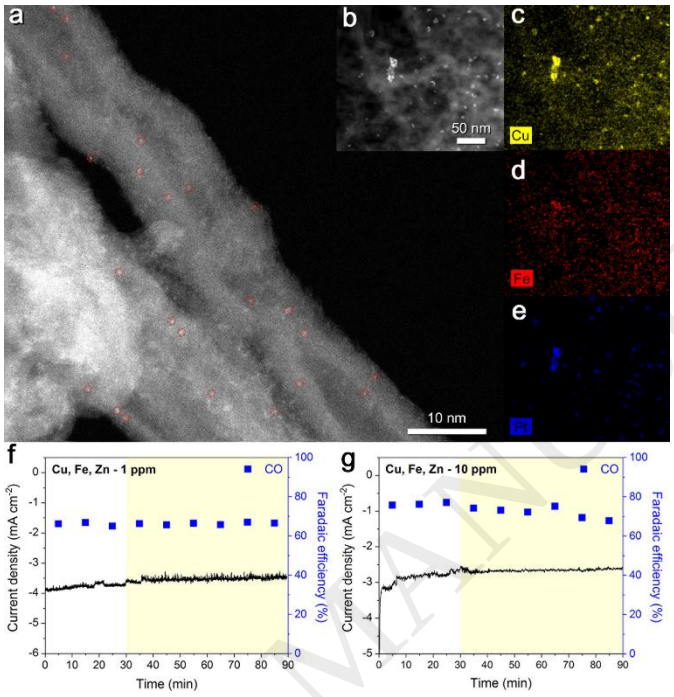

Fig. 6 Durability of the ball mill N-CNT catalyst. Surface of the post-reaction ball mill N-CNT catalyst observed by (a and b) HAADF-STEM images (the red circles indicate the bright spots on ball mill N-CNT, which were induced by metal particles) and EDX mapping analyses of (c) Cu (yellow), (d) Fe (red), and (e) Pt (blue). The durability of ball mill N-CNT towards metal impurities was examined upon *in situ* injection of (f) a solution containing 1 ppm of Cu, Fe, and Zn, and (g) a solution containing 10 ppm of Cu, Fe, and Zn in CO_2-bubbled 0.5 M $KHCO_3$ at −0.46 V (*vs.* RHE) (the black line, blue square, and yellow background represent current density, CO Faradaic efficiency, and behaviour after the injection of stock solution, respectively.).

Table 1 Composition of various impurities contained in tap water service in Seoul, Korea and their standard reduction potentials.

	Tap water (ppm)	Standard reduction potential[a]		Group[b]
K	2.82	$K^+(aq) + e^- \rightarrow K(s)$	$E^0 = -2.93$	i
Ca	18.23	$Ca^{2+}(aq) + 2e^- \rightarrow Ca(s)$	$E^0 = -2.84$	
Na	9.48	$Na^+(aq) + e^- \rightarrow Na(s)$	$E^0 = -2.71$	
Mg	4.40	$Mg^{2+}(aq) + 2e^- \rightarrow Mg(s)$	$E^0 = -2.36$	
Cu	0.02	$Cu^+(aq) + e^- \rightarrow Cu(s)$	$E^0 = +0.52$	ii
		$Cu^{2+}(aq) + 2e^- \rightarrow Cu(s)$	$E^0 = +0.34$	
		$Cu^{2+}(aq) + e^- \rightarrow Cu^+(aq)$	$E^0 = +0.16$	
Fe	0.04	$Fe^{2+}(aq) + 2e^- \rightarrow Fe(s)$	$E^0 = -0.44$	
		$Fe^{3+}(aq) + e^- \rightarrow Fe^{2+}(aq)$	$E^0 = -0.04$	
		$Fe^{3+}(aq) + 3e^- \rightarrow Fe(s)$	$E^0 = +0.77$	
Zn	0.06	$Zn^{2+}(aq) + 2e^- \rightarrow Zn(s)$	$E^0 = -0.76$	
Si	2.27	Usually not ionized		iii
Al	0.01	Anion state under neutral to alkali condition		

[a]The data of standard reduction potentials (298K) is taken mainly from "Electrochemical Methods: Fundamentals and Applications".

[b]Impurities are classified as each group based on the possibility of deposition under CO_2 reduction. Group i cannot be deposited by their negative reduction potential. Group ii can be deposited. Group iii can be excluded due to their states under experimental condition.

Supplementary Information

Supplementary Figures

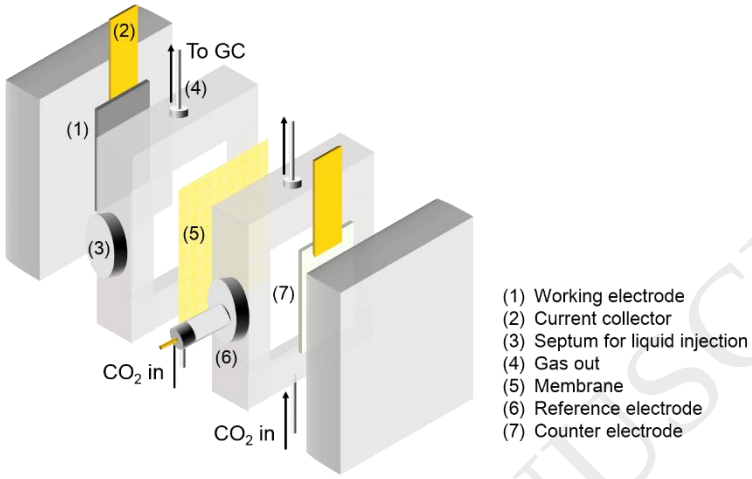

Fig. S1 A scheme of two-compartment customized electrochemical cell

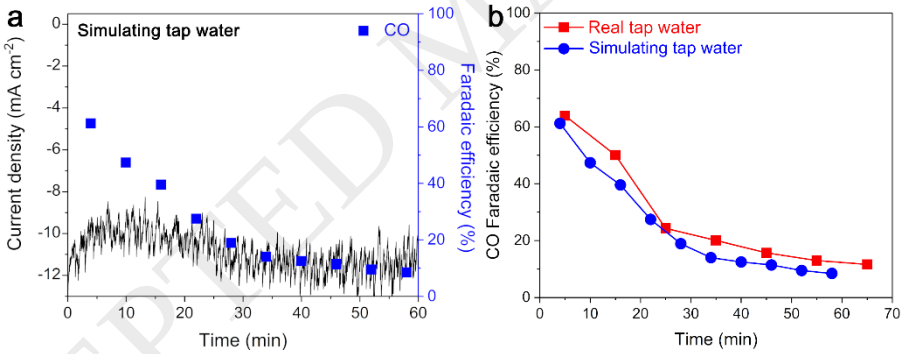

Fig. S2 Performance behaviours of a Ag electrode observed in two types of tap water. (a) CO_2 reduction activity in a CO_2-bubbled 0.5 M $KHCO_3$ electrolyte at −1.0 V (*vs.* RHE) using simulating tap water (the black line and blue square represent current density and CO Faradaic efficiency, respectively). (b) Comparisons of CO Faradaic efficiencies in real tap water (the red square) and in simulating tap water (the blue circle).

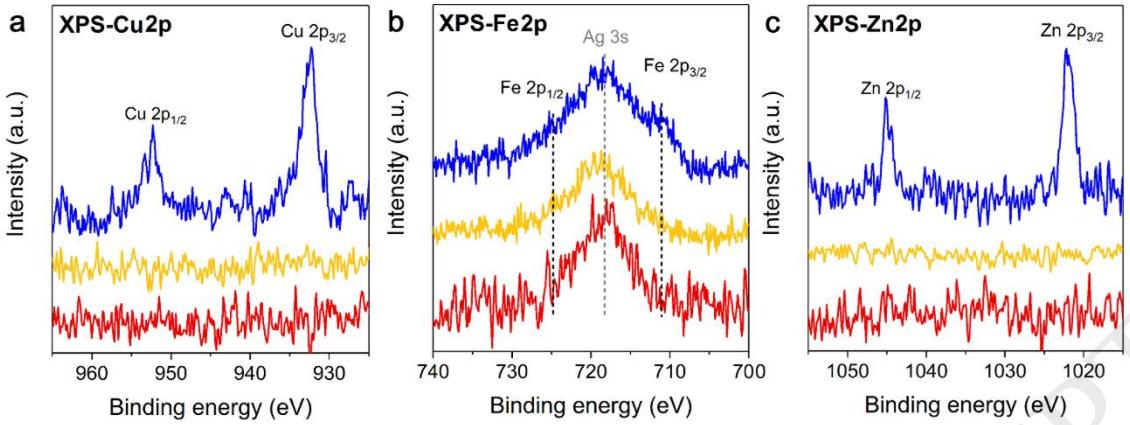

Fig. S3 Different properties of a Ag electrode after reaction in tap water. The surfaces of pristine Ag foil (red line) and post-reaction Ag foils in deionized water (yellow line) and tap water (blue line) were analyzed by XPS (a) −Cu_{2p}, (b) −Fe_{2p}, and (c) −Zn_{2p}.

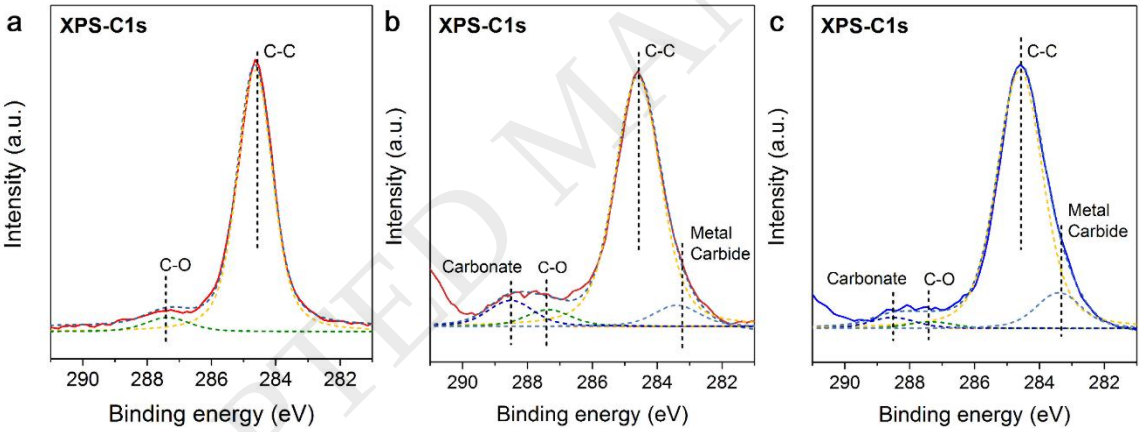

Fig. S4 Surface properties of a Ag electrode depending on reaction conditions. The surfaces of (a) pristine Ag foil (red line) and post-reaction Ag foils in (b) deionized water (brown line) and (c) tap water (blue line) were analyzed by XPS−C_{1s}.

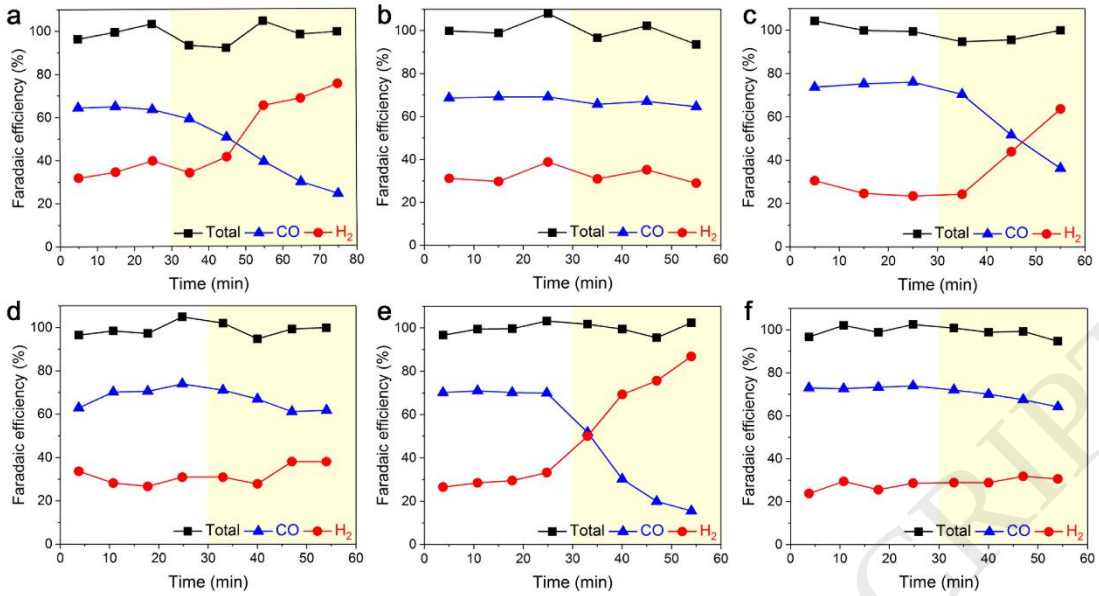

Fig. S5 Faradaic efficiency trends of a Ag electrode with respect to the electrolyte water conditions. The observed performance profile after *in situ* injection of various stock solutions in the CO_2-bubbled 0.5 M $KHCO_3$ electrolyte at −1.0 V (*vs.* RHE) using deionized water: (a) a solution for simulating the tap water environment, containing group i (*i.e.*, Ca, Na, and Mg) and group ii (*i.e.*, Cu, Fe, and Zn) elements, (b) a solution containing group i impurities (c) a solution containing group ii impurities, and three solutions containing (d) Cu, (e) Fe, and (f) Zn (the black square, blue triangle, and red circle represent total, CO, and H_2 Faradaic efficiency, respectively. Yellow background represents Faradaic efficiency behaviour after the injection of stock solution.).

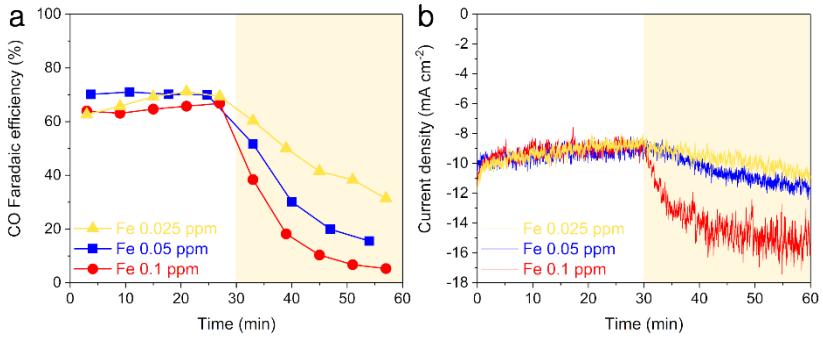

Fig. S6 Performance trends of a Ag electrode with respect to the metal impurity concentrations. The observed performance profile after *in situ* injection of various stock solutions containing different Fe concentrations (*i.e.*, 0.025, 0.05, and 0.1 ppm) in the CO_2-bubbled 0.5 M $KHCO_3$ electrolyte at −1.0 V (*vs.* RHE): comparisons of (a) CO Faradaic efficiencies and (b) current densities depending on the injected Fe concentrations (the yellow, blue, and red colors represent the results from different Fe concentrations of 0.025, 0.05, and 0.1 ppm, respectively. Yellow background represents performance behaviour after the injection of stock solution.).

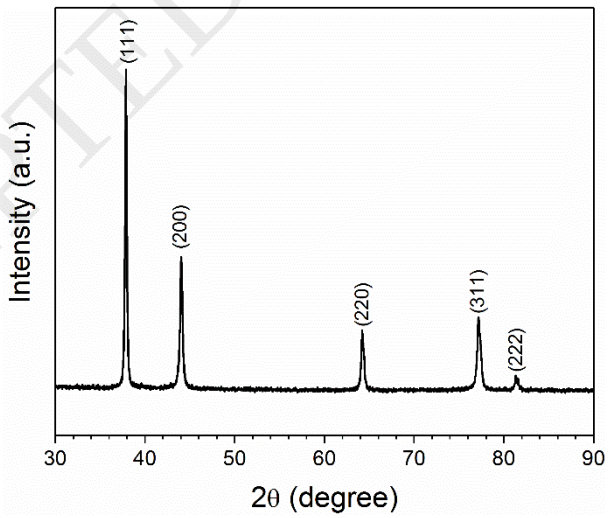

Fig. S7 XRD pattern of a Ag foil.

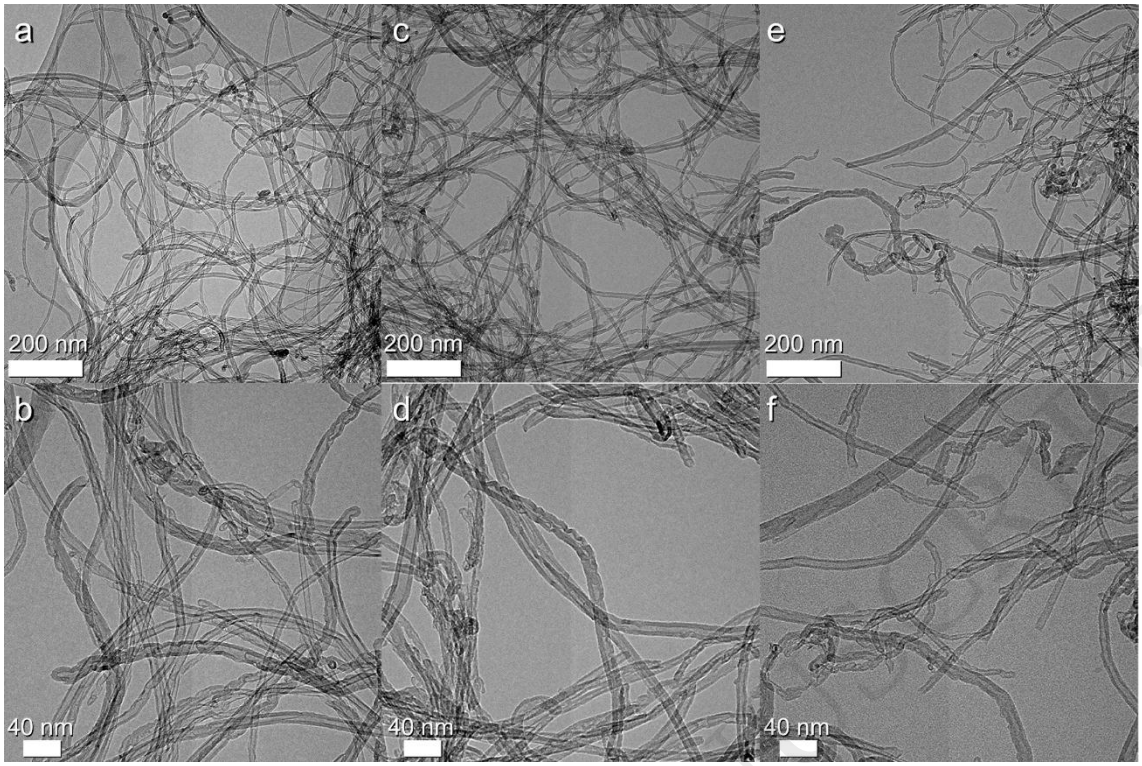

Fig. S8 Morphology of the prepared CNT catalysts. Morphology of (a and b) N-CNT, (c and d) N-oxi-CNT, and (e and f) ball mill N-CNT as observed under a TEM.

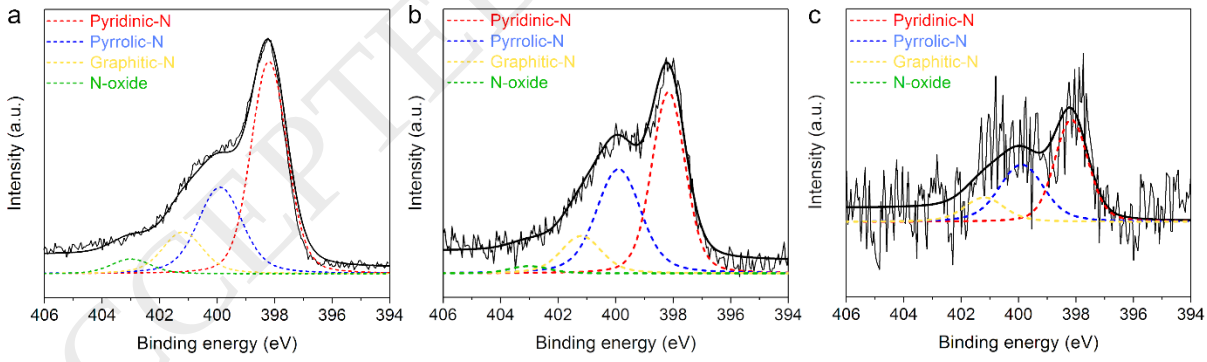

Fig. S9 The chemical nature of doped N in the prepared CNT catalysts as analyzed using XPS−N_{1s}. Deconvolution of N_{1s} peaks of (a) ball mill N-CNT (b) N-oxi-CNT, and (c) N-CNT.

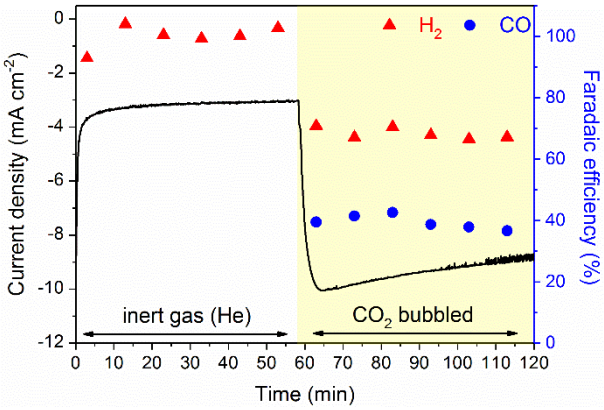

Fig. S10 Demonstration of carbon source for produced CO. The catalytic performance of ball mill N-CNT under He and CO_2 bubbled 0.5 M $KHCO_3$ at −1.35 V (*vs*. Ag/AgCl). Current density (black line), H_2 Faradaic efficiency (red triangle) and CO Faradaic efficiency (blue circle) depend on the type of supplied gas: without (white background) and with CO_2 (yellow background).

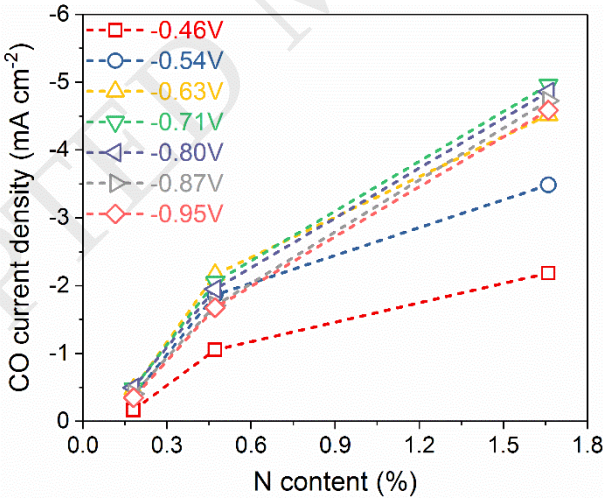

Fig. S11 Correlation of catalytic performance with doped N content in the prepared CNT catalysts.

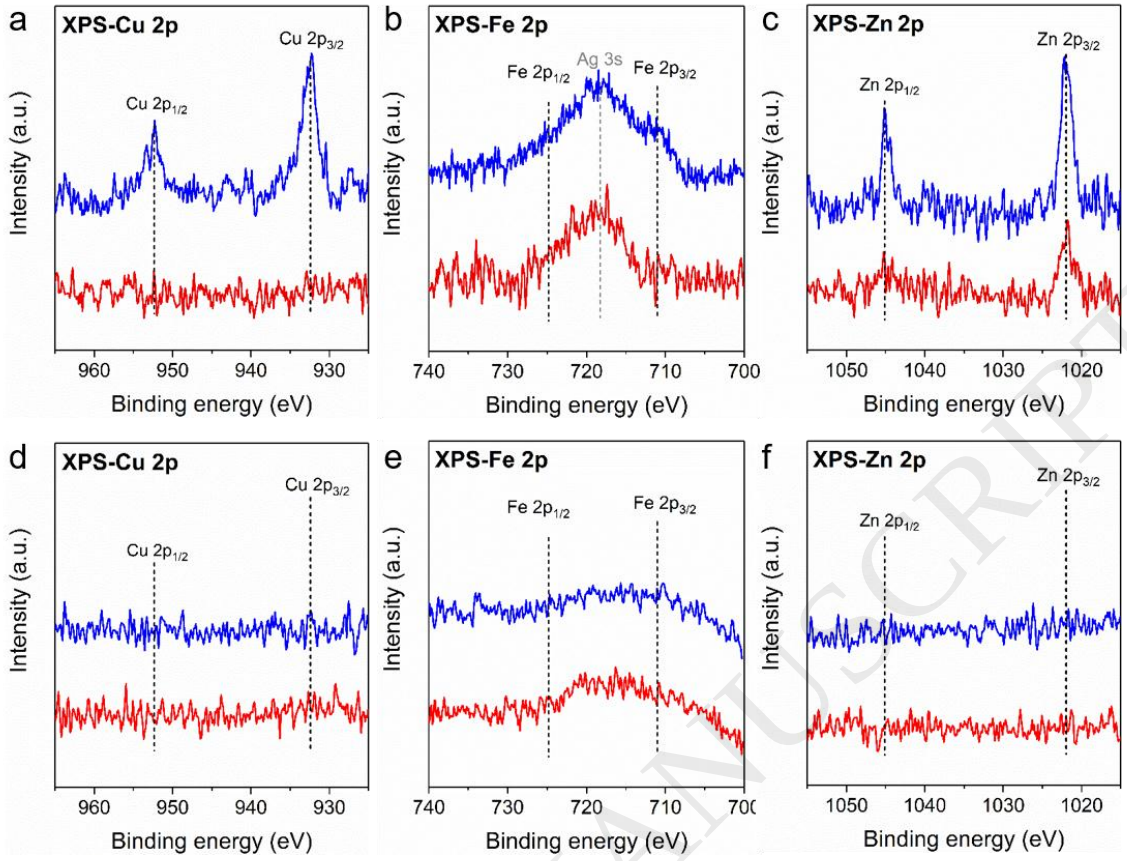

Fig. S12 Surface properties of (a)-(c) Ag foil and (d)-(f) ball mill N-CNT depending on the different applied potentials, *i.e.*, −0.46 V_{RHE} (blue) and −1.0 V_{RHE} (red). CO_2RR performed during 2 h. The surfaces of post-reaction Ag foils at −0.46 V_{RHE} (blue) and −1.0 V_{RHE} (red) were analyzed by XPS (a) $-Cu_{2p}$, (b) $-Fe_{2p}$, and (c) $-Zn_{2p}$, respectively. The surfaces of post-reaction ball mill N-CNT at −0.46 V_{RHE} (blue) and −1.0 V_{RHE} (red) were also analyzed by XPS (d) $-Cu_{2p}$, (e) $-Fe_{2p}$, and (f) $-Zn_{2p}$, respectively.

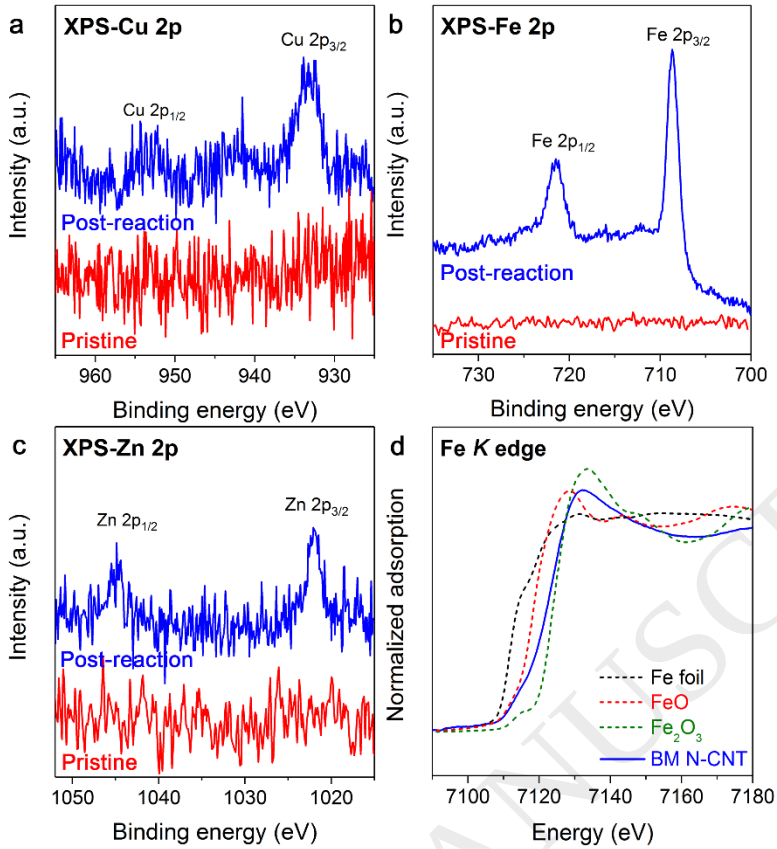

Fig. S13 Surface of ball mill N-CNT after long-term operation in a tap water electrolyte. The surfaces of pristine ball mill N-CNT (red line) and post-reaction ball mill N-CNT (blue line) were analyzed by XPS (a) $-Cu_{2p}$, (b) $-Fe_{2p}$, and (c) $-Zn_{2p}$. (d) The oxidation state of Fe on ball mill CNT was analyzed by the XANES Fe *K*-edge.

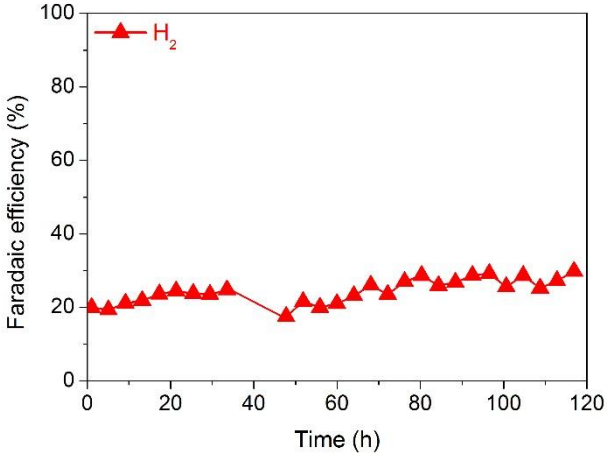

Fig. S14 H_2 Faradaic efficiency during the long-term operation of ball mill N-CNT in CO_2-bubbled 0.5 M $KHCO_3$ using tap water at −0.44 V (*vs.* RHE).

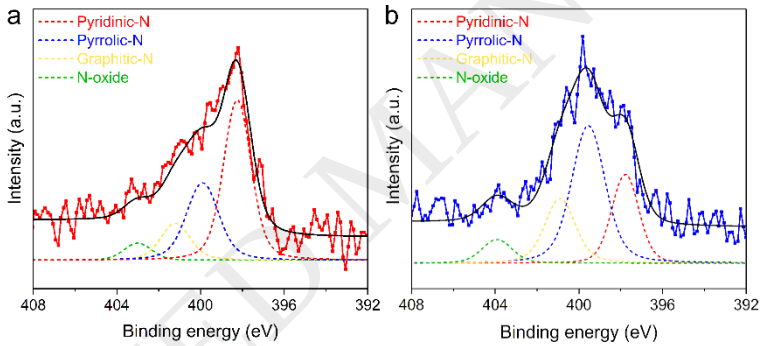

Fig. S15 The nature of N species of ball mill N-CNT after long-term operation in a tap water electrolyte. XPS−N_{1s} spectra of (a) pristine ball mill N-CNT (red line) and (b) post-reaction (blue line) ball mill N-CNT.

Supplementary Tables

Table S1 Comparison of CO_2 reduction stability on various catalysts for CO_2-to-CO production in similar operating conditions.

	Catalysts	Electrolyte			Operating potential (V_{RHE})	Operating time[a] (h)	Current density (mA cm^{-2})[b]	FE_{CO} (%)[b]	Ref.
		Concentration	Water	Precursor Purity					
Metal	AuFe alloy	0.5 M $KHCO_3$	Ultrapure water	N/A	−0.5	90	−11.05	97.6	[1]
	Au nanoparticle	0.5 M $NaHCO_3$	Deionized water	99.999%	−0.5	12	−12[b]	94	[2]
	Au needle	0.5 M $KHCO_3$	Deionized water	N/A	−0.3	8	−22	95	[3]
	Tri-Ag-NP	0.1 M $KHCO_3$	Deionized water	>99.99%	−0.856	14	−1.25	97	[4]
	Nanoporous Ag	0.5 M $KHCO_3$	Deionized water	>99.99%	−0.50	8	−9	87	[5]
	Hexagonal Zn	0.5 M KCl	Deionized water	≥ 99.0%	−1.05	30	−5	95	[6]
	RE-Zn	0.5 M $KHCO_3$	Deionized water	≥99.99%	−1.10	20	−8	80	[7]
	Cu-In	0.1 M $KHCO_3$	Deionized water	99.99%	−0.6	7	−0.7	85	[8]
Metal Contained Carbon	CoPc/CNT	0.1 M $KHCO_3$	Deionized water	N/A	−0.63	10	−10	90	[9]
	A-Ni-NSG	0.5 M $KHCO_3$	Deionized water	99.7%	−0.72	100	−22	98	[10]
	ZnN_x/C	0.5 M $KHCO_3$	Deionized water	analytical grade	−0.43	75	−4.8	95	[11]
	Co-N_2	0.5 M $KHCO_3$	Deionized water	N/A	−0.63	60	−18.1	94	[12]
	Ni SAs/N-C	0.5 M $KHCO_3$	Deionized water	N/A	−1.00	60	−10.48	71.9	[13]
Matal Fre e Carbon	3D graphene	0.1 M $KHCO_3$	N/A	N/A	−0.58	5	−1.5	85	[14]
	N-CNT	0.5 M $NaHCO_3$	Distilled Water	N/A	−0.9	60	−5.8	85	[15]
	Ball mill N-CNT	**0.5 M $KHCO_3$**	**Tap water**	**99.7%**	**−0.44**	**120**	**−3**	**70**	**This study**

[a]The operating time when both the CO Faradaic efficiency and current density results are presented (Since constant current density may not be accompanied by a constant CO Faradaic efficiency, we exclude the case where only current density is indicated).
[b]The value which is not mentioned in the article is derived from the graphical results.
[c]The unit for this current density is A g^{-1}.

Table S2 The composition and concentration of the stock solution for simulating the tap water.

	Precursor	Target concentration of metal (ppm)	Concentration of stock solution (μg ml^{-1})
Ca	$CaCl_2$	22	1256.09
Na	$NaHCO_3$	10	733.04
Mg	$MgCl_2$	4	319.78
Cu	$CuCl_2 \cdot 2H_2O$	0.05	2.68
Fe	$FeCl_2$	0.05	2.27
Zn	$ZnCl_2$	0.05	2.08
Cl[a]	KCl	26	524.5

[a]Amount of Cl inevitably contained in the stock solution for simulating the tap water. Thus, the stock solution only containing Cl^- was also prepared at the above concentration.

Table S3 Compositions of the prepared CNT catalysts obtained from elemental analyzer.

at.%	Ball mill CNT	N-oxi-CNT	N-CNT	CNT
N	1.66	0.47	0.18	0.01
C	96.65	96.57	98.57	98.49
H	0.63	2.08	0.28	0.91
O	1.06	0.88	0.96	0.58

References.

[1] K. Sun, T. Cheng, L. Wu, Y. Hu, J. Zhou, A. Maclennan, Z. Jiang, Y. Gao, W.A. Goddard, Z. Wang, Ultrahigh Mass Activity for Carbon Dioxide Reduction Enabled by Gold–Iron Core–Shell Nanoparticles, J. Am. Chem. Soc., 139 (2017) 15608-15611. https://doi.org/10.1021/jacs.7b09251.

[2] X. Feng, K. Jiang, S. Fan, M.W. Kanan, Grain Boundary Dependent CO_2 Electroreduction Activity, J. Am. Chem. Soc., 137 (2015) 4606-4609. https://doi.org/10.1021/ja5130513.

[3] M. Liu, Y. Pang, B. Zhang, P. De Luna, O. Voznyy, J. Xu, X. Zheng, C.T. Dinh, F. Fan, C. Cao, F.P.G. de Arquer, T.S. Safaei, A. Mepham, A. Klinkova, E. Kumacheva, T. Filleter, D. Sinton, S.O. Kelley, E.H. Sargent, Enhanced electrocatalytic CO_2 reduction via field-induced reagent concentration, Nature, 537 (2016) 382-386. https://doi.org/10.1038/nature19060.

[4] S. Liu, H. Tao, L. Zeng, Q. Liu, Z. Xu, Q. Liu, J.-L. Luo, Shape-Dependent Electrocatalytic Reduction of CO_2 to CO on Triangular Silver Nanoplates, J. Am. Chem. Soc., 139 (2017) 2160-2163. https://doi.org/10.1021/jacs.6b12103.

[5] Q. Lu, J. Rosen, Y. Zhou, G.S. Hutchings, Y.C. Kimmel, J.G. Chen, F. Jiao, A selective and efficient electrocatalyst for carbon dioxide reduction, Nat. Commun., 5 (2014) 3242-3247. https://doi.org/10.1038/ncomms4242.

[6] D.H. Won, H. Shin, J. Koh, J. Chung, H.S. Lee, H. Kim, S.I. Woo, Highly Efficient, Selective, and Stable CO_2 Electroreduction on a Hexagonal Zn Catalyst, Angew. Chem. Int. Ed., 55 (2016) 9297-9300. https://doi.org/10.1002/anie.201602888.

[7] D.L.T. Nguyen, M.S. Jee, D.H. Won, H. Jung, H.-S. Oh, B.K. Min, Y.J. Hwang, Selective CO_2 Reduction on Zinc Electrocatalyst: The Effect of Zinc Oxidation State Induced by Pretreatment Environment, ACS Sustainable Chem. Eng., 5 (2017) 11377-11386. https://doi.org/10.1021/acssuschemeng.7b02460.

[8] S. Rasul, D.H. Anjum, A. Jedidi, Y. Minenkov, L. Cavallo, K. Takanabe, A Highly

Selective Copper–Indium Bimetallic Electrocatalyst for the Electrochemical Reduction of Aqueous CO_2 to CO, Angew. Chem. Int. Ed., 54 (2015) 2146-2150. https://doi.org/10.1002/anie.201410233.

[9] X. Zhang, Z.S. Wu, X. Zhang, L.W. Li, Y.Y. Li, H.M. Xu, X.X. Li, X.L. Yu, Z.S. Zhang, Y.Y. Liang, H.L. Wang, Highly selective and active CO_2 reduction electro-catalysts based on cobalt phthalocyanine/carbon nanotube hybrid structures, Nat. Commun., 8 (2017) 14675-14682. https://doi.org/10.1038/ncomms14675.

[10] H.B. Yang, S.-F. Hung, S. Liu, K. Yuan, S. Miao, L. Zhang, X. Huang, H.-Y. Wang, W. Cai, R. Chen, J. Gao, X. Yang, W. Chen, Y. Huang, H.M. Chen, C.M. Li, T. Zhang, B. Liu, Atomically dispersed Ni(i) as the active site for electrochemical CO_2 reduction, Nat. Energy, 3 (2018) 140-147. https://doi.org/10.1038/s41560-017-0078-8.

[11] F. Yang, P. Song, X. Liu, B. Mei, W. Xing, Z. Jiang, L. Gu, W. Xu, Highly Efficient CO_2 Electroreduction on ZnN_4-based Single-Atom Catalyst, Angew. Chem. Int. Ed., (2018). https://doi.org/10.1002/anie.201805871.

[12] X. Wang, Z. Chen, X. Zhao, T. Yao, W. Chen, R. You, C. Zhao, G. Wu, J. Wang, W. Huang, J. Yang, X. Hong, S. Wei, Y. Wu, Y. Li, Regulation of Coordination Number over Single Co Sites: Triggering the Efficient Electroreduction of CO_2, Angew. Chem. Int. Ed., 57 (2018) 1944-1948. https://doi.org/10.1002/anie.201712451.

[13] C. Zhao, X. Dai, T. Yao, W. Chen, X. Wang, J. Wang, J. Yang, S. Wei, Y. Wu, Y. Li, Ionic Exchange of Metal–Organic Frameworks to Access Single Nickel Sites for Efficient Electroreduction of CO_2, J. Am. Chem. Soc., 139 (2017) 8078-8081. https://doi.org/10.1021/jacs.7b02736.

[14] J. Wu, M. Liu, P.P. Sharma, R.M. Yadav, L. Ma, Y. Yang, X. Zou, X.-D. Zhou, R. Vajtai, B.I. Yakobson, J. Lou, P.M. Ajayan, Incorporation of Nitrogen Defects for Efficient Reduction of CO_2 via Two-Electron Pathway on Three-Dimensional Graphene Foam, Nano

Letters, 16 (2016) 466-470. https://doi.org/10.1021/acs.nanolett.5b04123.

[15] J. Xu, Y. Kan, R. Huang, B. Zhang, B. Wang, K.H. Wu, Y. Lin, X. Sun, Q. Li, G. Centi, D. Su, Revealing the Origin of Activity in Nitrogen-Doped Nanocarbons towards Electrocatalytic Reduction of Carbon Dioxide, ChemSusChem, 9 (2016) 1085-1089. https://doi.org/10.1002/cssc.201600202.